Geomorphology 392 (2021) 107927

Contents lists available at ScienceDirect

Geomorphology

journal homepage: www.elsevier.com/locate/geomorph

Complex relationships between surface topography, ground motion, and cover sediments in covered karst, west-central Florida, USA

Tonian Robinson [a,*], Bruce Rodgers [b], Talib Oliver-Cabrera [c], Christine Downs [a], Sarah Kruse [a], Shimon Wdowinski [c], Boya Zhang [c], Sajad Jazayeri [a], Sanaz Esmaeili [a], Henok Kiflu [a]

[a] School of Geosciences, University of South Florida, Tampa, FL, USA
[b] Bruce A. Rodgers, P.G., P.A, USA
[c] Department of Earth and Environment, Florida International University, Miami, FL, USA

ARTICLE INFO

Article history:
Received 1 April 2021
Received in revised form 24 August 2021
Accepted 25 August 2021
Available online 28 August 2021

Keywords:
Sinkholes
Hazard
Geophysics
PSInSAR

ABSTRACT

Sinkhole processes can be more complicated than vertical drainage or collapse of sediments into an underlying limestone void. To better understand the relationships between surface and underlying karst structures, geodetic and geophysical methods were applied to high-resolution mapping of active sinkhole features in covered karst, west-central Florida, USA. Cracks in a pool house at the Sandhill Scout Reservation prompted surface and subsurface investigations in a grassy open field with a distinct ~60-m diameter topographic low west of the pool area. Beneath the smooth topographic low, ground-penetrating radar (GPR) with limited penetration (up to 6 m depth) shows incongruent smaller-scale (~5–20 m) variability in a horizon draping the limestone surface. Electrical Resistivity Tomography (ERT) profiles provide a broader overview of the underlying karst system (to depths ~25–36 m) and show possible voids in the limestone bedrock beneath a local topographic high. Persistent Scatterer Interferometric Synthetic Aperture Radar (PSInSAR) analysis of ~2 yr of TerraSAR-X satellite data from two corner-reflectors installed in the topographic low reveals a 1 mm/yr subsidence rate on the flank of the topographic low but stability in its center. This suggests that subsidence has halted in the central topographic low and may be occurring on smaller scales elsewhere within the survey area. The data suggest that non-vertical fluxes of sediment significantly smooth surface topography relative to underlying heterogeneities and that activity migrates within complex systems. Our results also illustrate the benefits of corner reflector installations for resolving subsidence in vegetated environments. The 1-mm/yr rate of motion on the grassy field could not be resolved with InSAR before reflector installation.

1. Introduction

Sinkholes are geological hazards that threaten urban areas in west-central Florida, where their formation is accelerated by anthropogenic activities such as excessive groundwater pumping and land development (Tihansky, 1999; Tihansky and Knochenmus, 2001; Aurit et al., 2013; Xiao et al., 2016). Florida's bedrock consists of carbonates that are susceptible to dissolution processes caused by acidic rain percolation into the subsurface (Tihansky, 1999). In the covered-karst of west-central Florida, sinkholes are often associated with the suffosion of sandy overburden sediments into open fissures. This process, also called raveling, leads to surface subsidence related to nearby voids (Tihansky, 1999). The growing topographic depressions are described as cover-subsidence sinkholes. Because sinkholes cause significant property damage and even loss of life, an improved understanding of sinkhole processes is societally important. Improved understanding requires better mapping of structure and evolution, particularly in the covered karst of many heavily developed areas in west-central Florida.

Cover-subsidence sinkholes are commonly depicted as downward sagging of the land surface above near-vertical conduits connected to growing underlying subsurface voids (e.g., Tihansky, 1999). However, this relatively simple image fails to describe some of the complexities observed at sinkholes in west-central Florida. Tihansky (1999) shows that the top of limestone is pocketed with depressions and fractures on scales of ~1–5 m, observed continuously over distances of hundreds of meters in some west-central Florida quarries. In contrast, surface depressions identified as sinkholes are more isolated and widely spaced and typically a few meters or larger in dimension. In west-central Florida, Kiflu (2013) found that raveling in surface sediments is likely to be laterally offset, on the order of a few meters, from underlying voids/weak zones. These results suggest that many raveling zones are more complex and inclined rather than vertical. Downs (2017) observed additional complexity on scales of tens of meters, with topographic

* Corresponding author.
E-mail address: tonianr@usf.edu (T. Robinson).

https://doi.org/10.1016/j.geomorph.2021.107927
0169-555X/

highs in hummocky wetlands in west-central Florida not necessarily underlain by limestone pinnacles but also by zones of thick cover sediments. Thus, surface topography does not necessarily show a simple relationship to the top of buried limestone.

This paper documents complexities in sinkhole structure on scales from meters to a few hundred meters observed at a study site with documented sinkhole activity, yet minimal development, in Hernando County, Florida. This work is a part of a larger study by Oliver-Cabrera

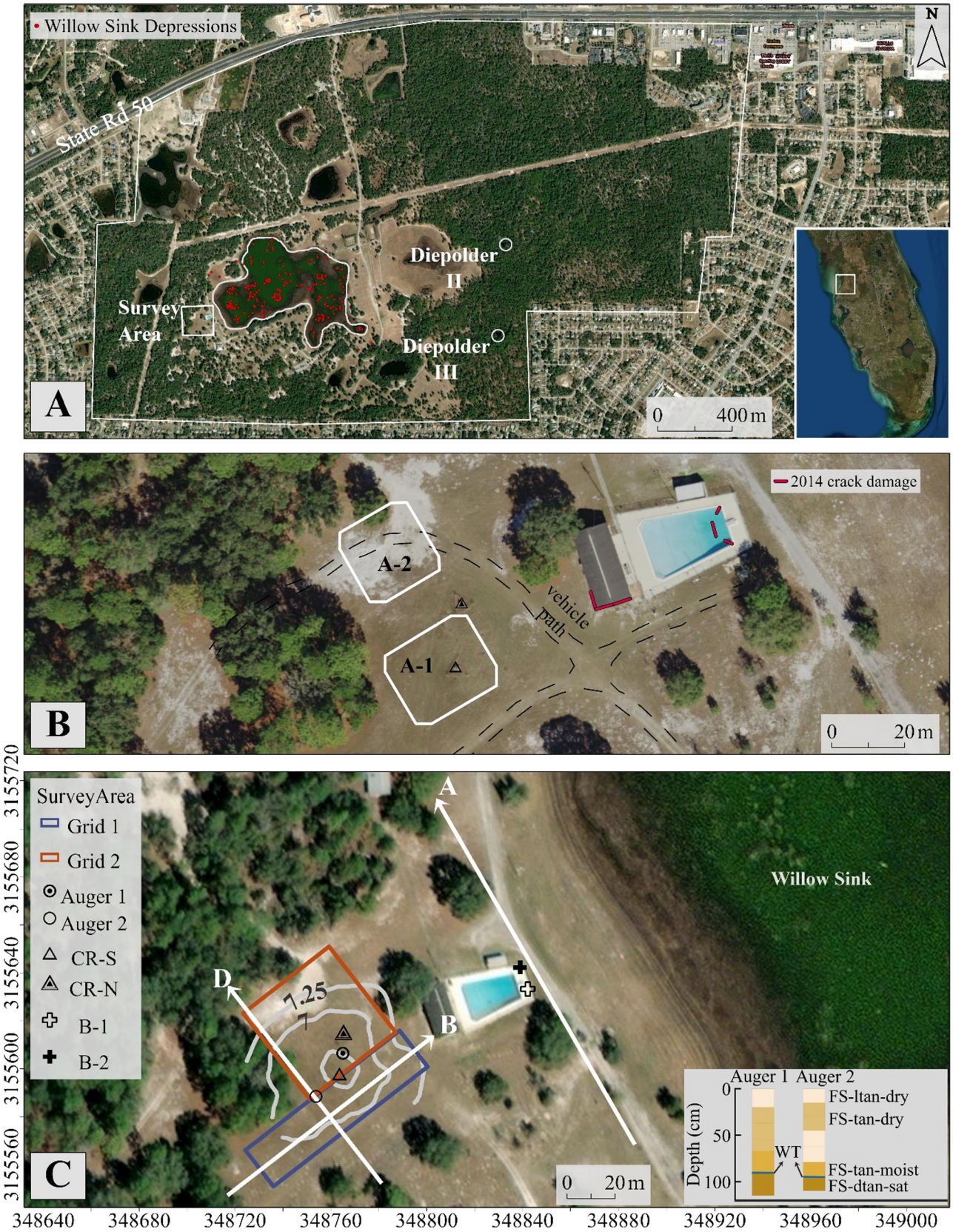

et al. (2021) that demonstrates the applicability of using PSInSAR to detect sinkhole-related deformation in west-central Florida. Oliver-Cabrera et al. (2021) found that buildings and roads are ideal persistent scatters in this highly vegetated sub-tropical setting. Thus on the grassy field study site described here, identifying subsidence from InSAR required the installation of corner reflectors. Simultaneously, the open grassy field permits high-resolution geophysical data acquisition and examination of relationships between surface topography, cover sediments, and ground motions.

Research at the Sandhill Scout Reservation within the rapidly urbanizing west-central Florida was prompted after visible cracks appeared in a nearby swimming pool and pool house (Fig. 1B). A two-year-long PSInSAR time-series tracks the surficial deformation at two corner reflectors installed in a ~60-m diameter topographic low. We combine the PSInSAR data with terrestrial LiDAR, structure from motion (SfM) photogrammetry, and subsurface mapping using geophysical methods (GPR and ERT) for high-resolution comparison of surface elevations and subsidence with underlying sinkhole-related structures. This combination of 2D surface and subsurface imaging with accurate deformation monitoring from PSInSAR has not, to our knowledge, been applied to investigate sinkhole deformation in Florida. Key findings are that (a) smooth surface topography at larger depressions (~60 m) masks shorter-scale (~5–20 m) structures in karst cover sediments, and (b) faster subsidence is currently observed on the flank of the topographic low than in the center of the depression. The results suggest that lateral fluxes in cover sediments serve to smooth topography and that current subsidence is not apparent in the surface topography.

2. Sinkhole mapping and monitoring techniques

A wide variety of techniques have been applied in studies of sinkhole structure and deformation in carbonate and evaporite karst terranes. These works cover:

- Remote sensing techniques such as terrestrial laser scanning (TLS), also known as Light Detection and Ranging (LiDAR), Structure from Motion (SfM) photogrammetry, and Interferometric Synthetic Aperture Radar (InSAR) used to map and monitor surface deformation and to develop automated approaches for determining patterns related to sinkhole formation (Doctor and Young, 2013; Nof et al., 2013; Zhu et al., 2014; Yechieli et al., 2015; Kim et al., 2019; Nof et al., 2019; Shi et al., 2019; Zumpano et al., 2019).
- Geophysical methods such as ground penetrating radar (GPR) (Rodriguez et al., 2014; Fabregat et al., 2019; Ronen et al., 2019), Electrical Resistivity Tomography (ERT) (Carbonel et al., 2014; Andrade-Gómez et al., 2019; Youssef et al., 2020), seismic methods (Dahm et al., 2011; Breithaupt, 2016), and self-potential (SP) (Jardani et al., 2006; Bumpus and Kruse, 2014) that provide specific information related to the physical and electrical structure of karst terranes.
- Hydrogeological approaches include potentiometric surface monitoring and tracer testing and hydrogeochemical analyses that are usually contingent on the availability of subsurface conduits, streams, or cavern systems for fluid transport (Gutiérrez et al., 2008; Martel et al., 2018; Burke et al., 2020; Soldo et al., 2020).
- Trenching, though an invasive method, can detect the precise location of sinkhole boundaries; this reduces the uncertainty usually associated with geophysical methods (Gutiérrez et al., 2011, 2018). It can also provide information on a sinkhole's past and present behavior, age, deformation magnitude, and subsidence mechanisms that resulted in collapse (Fabregat et al., 2017, 2019; Sevil et al., 2017).
- High-precision leveling is known for measuring relative-vertical changes at point locations with submillimeter accuracy. It has been successfully used to pinpoint the limits of actively subsiding areas and provide spatiotemporal variability in these zones (Sevil et al., 2017, 2021; Benito-Calvo et al., 2018; Desir et al., 2018). This technique has limited spatial coverage and is best supplemented with LIDAR/TLS (Benito-Calvo et al., 2018; Gutiérrez et al., 2019; Sevil et al., 2021) to allow widespread monitoring of subsidence patterns.
- Geospatial analyses and spatial statistics for developing sinkhole risk and probability models (Florea, 2005; Brinkmann et al., 2008; Galve et al., 2008, 2009a, 2009b, 2011; Doctor and Doctor, 2012; Al-Kouri et al., 2013; Ozdemir, 2015; Cahalan and Milewski, 2018; Zhu et al., 2020). Below, we review the techniques used in this study.

2.1. Surface elevation and deformation measurements

LiDAR and SfM photogrammetry are remote sensing techniques that use high-resolution topographic measurements to create topographic maps or 3D surfaces of terrestrial terrains (James et al., 2017; Westoby et al., 2012). Photogrammetry has been applied to produce a 5 cm vertical resolution 3D elevation model of fast-forming 20-m deep sinkholes within the Dead Sea's sparsely vegetated arid deposits (Al-Halbouni et al., 2017). Ground-based LiDAR has been extensively used to monitor surface deformation; however, relatively few studies have been applied to sinkholes. Benito-Calvo et al. (2018) used LiDAR to monitor the surface deformation of three active sinkholes (depths 4–15 m) in an evaporite karst terrane in Spain, where a spatial resolution of 7–12 mm was achieved with reported errors between 2 and 14 mm.

2.2. Satellite imaging

Many studies show that time-series InSAR can monitor deformation caused by sinkholes; however, most study sites are located in sparsely vegetated areas such as the Dead Sea and Texas (Baer et al., 2002, 2018; Nof et al., 2013, 2019; Kim et al., 2019; Shi et al., 2019). In contrast to these arid settings, Oliver-Cabrera (2018) and Oliver-Cabrera et al. (2020, 2021) found that monitoring sinkholes with satellite radar in humid, vegetated west-central Florida requires analysis of persistent scatterers (PSs) from buildings and roads. PSInSAR identifies and exploits point scatterers (usually smaller than the SAR pixel) with consistent high coherency over time to create time-series showing localized subsidence (Bell et al., 2008; Crosetto et al., 2016; Osmanoğlu et al., 2016). With PSInSAR, submillimeter changes have been detected for tracking small-scale movements (up to ~15 mm/yr) related to sinkhole deformation in urban areas (Oliver-Cabrera, 2018; Malinowska et al., 2019; Busetti et al., 2020).

We note there are specific circumstances in which sinkhole deformation could be monitored in vegetated areas. In Bayou Corne, Louisiana, Jones and Blom (2014) used L-Band (23.8 cm wavelength) SAR to monitor a large cavity (110 m-diameter) where a precursory displacement of up to 26 cm was captured before sinkhole formation. However, this application would not be reliable for sinkhole monitoring in west-

Fig. 1. Overview of Sandhill Reservation. A: Inset shows the location in west-central Florida. Cave diving locations Diepolder II and III are vertical conduits that lead to large open caves at 90–110 m depth. The Survey area box shows the location of the middle and bottom figures. B: White boxes show penetrometer data grids A-1 and A-2. Black dashed lines show frequent vehicle paths. Red lines indicate visible cracks found within the pool and poolhouse in 2014. C: Survey area with labeled Grids 1 and 2 over which GPR data were acquired. Grid 1 is approximately 80 m by 20 m, and Grid 2, 40 m by 60 m. Both Grids 1 and 2 have 1-m line spacing. A, B, and D show GPR and ERT profiles, with arrows indicating the direction of increasing distance along each line. Circles show auger borings, where the water table was recorded at 90 cm depth below ground surface (Auger 1) and 95 cm depth (Auger 2) within sands. Auger results (bottom-right) show tan fine sand (FS) variability below the surface where *ltan* and *dtan* represent light and dark tan colors. Triangles show corner reflectors CR-N and CR-S installed within the survey area to improve InSAR resolution of vertical motions. Contour lines (0.25 m intervals) show elevation. Reflector CR-S sits at the topographic low illustrated by contour line 6.75 m.

central Florida, where sinkholes are predominantly 5 m in diameter with submillimeter deformation patterns (Xiao et al., 2016; Oliver-Cabrera et al., 2020).

2.3. Subsurface imaging

Geophysical methods have been used for decades to characterize karst environments (e.g., Chalikakis et al., 2011). Ground-penetrating radar (GPR) may resolve shallow collapsed openings to cavities, conduits, fractures, and structures within cover sediments, resolving features from cm-scale up to tens of meters. Water-filled holes can be identified by high dielectric contrasts (Gómez-Ortiz and Martín-Crespo, 2012). Gutiérrez et al. (2011) and Sevil et al. (2017) used GPR to map the structure of evaporite karst sinkholes in Spain. Kruse et al. (2006) used GPR to image in detail a 15-m sinkhole depression and underlying conduit. With GPR, however, penetration is limited if surface soils or sediments are conductive (Gómez-Ortiz and Martín-Crespo, 2012), and variable moisture conditions can influence imaging (Sevil et al., 2017).

Electrical Resistivity Tomography (ERT) can delineate boundaries within and thicknesses of units in a karst system (Zhou et al., 2002; Chalikakis et al., 2011; Cardarelli et al., 2014) and the structure of underlying aquifer systems (Andrade-Gómez et al., 2019). When applied to sinkhole investigations, ERT profiles tend to allow deeper imaging (tens of meters in depth) compared to typically less than 10 m for GPR (Sevil et al., 2017). ERT spatial resolution is lower, on the order of meters or more, and sharp contacts are blurred. The deeper penetration offers the possibility of imaging limestone voids (Frumkin et al., 2011; Martínez-Moreno et al., 2013). Because lithology, water content, and water composition affect resistivity readings, this technique frequently needs to be integrated with other methods (Cardarelli et al., 2014). Work from Kruse et al. (2006), Frumkin et al. (2011), Gómez-Ortiz and Martín-Crespo (2012), Kiflu (2013), Martínez-Moreno et al. (2013), Carbonel et al. (2014), Cardarelli et al. (2014), Kaufmann (2014), Fabregat et al. (2017), Sevil et al. (2017), Pazzi et al. (2018), and Hussain et al. (2020) show that a combination of geophysical methods is desirable to optimize the detection and delineation of sinkhole structures.

2.4. Integrated surface and subsurface studies

Literature that focuses on integrating high-resolution subsurface imaging and measured ground displacement to map the connections between surface deformation and the alignment of suffosion zones is limited. Here we list some works with similar approaches. Gutiérrez et al. (2011), Carbonel et al., 2015, Martel et al. (2018), and Busetti et al. (2020) used both geophysical techniques and InSAR with additional methods such as trenching (Carbonel et al., 2015), precision leveling (Gutiérrez et al., 2011; Busetti et al., 2020), and tracer tests and boreholes (Martel et al., 2018). These studies demonstrate that a combination of spatial and temporal techniques would be most beneficial in mitigating damages related to sinkhole formation. In regards to the scales of features imaged, Gutiérrez et al. (2011), Carbonel et al. (2015), and Busetti et al. (2020) focused on sinkholes tens of meters in size (similar to this study), while Martel et al. (2018) studied cavern systems hundreds of meters in length. In summary, these investigations show that an interdisciplinary approach, i.e., integrating geophysical and geodetic methods, is valuable for improving detection, forecasting, and effective monitoring of sinkhole development.

3. Study site geology

The Sand Hill Scout Reservation occupies about 5.2 km^2 of near-natural landscape in Hernando County, Florida (Fig. 1A). Residential communities bound the reservation to the south with State Road 50 on the north (Fig. 1A). The land is managed as a ranch or Scout camp, and disturbances to its natural existence are primarily related to isolated building construction. The reservation's geomorphology represents the final remaining preserve of a wet prairie terrane that once included about 4000 km^2 in a narrow band along Florida's western coast (Healy, 1975).

Three primary geologic formations are important to the property's surface terrain (Fig. 2). (1) The deepest of these, ~27 m below the land surface, is the Eocene age Ocala Limestone (Scott, 2011; Upchurch et al., 2018). The Ocala Limestone supports an extensive network of interconnecting caves, conduits, and cavities and is synonymous with the Floridan Aquifer System, one of the world's most productive aquifers (Miller, 1990). (2) Above the Ocala Limestone and separated by an unconformity is the Oligocene age Suwannee Limestone (Fig. 2). This is generally crystalline compared to the underlying Ocala formation and serves as a minable aggregate (Puri and Vernon, 1959). Dissolution within the Suwannee Limestone characteristically has symmetrical solution holes ranging up to 10 m in diameter (Rodgers, 2007). These shafts connect to a network of Ocala caves and conduits and are expressed on the surface by artesian springs and clear-water sinkholes (Purdum and Fernald, 1998). Two clear water sinkholes on the Sand Hill Scout Reservation, DiePolder II and DiePolder III (Fig. 1A), allow SCUBA access into the Floridan Aquifer within the Ocala Limestone. Other surficial water-filled sinkholes on the property communicate with the Floridan Aquifer System through quartz sand-filled shafts (Rodgers, 2007). The aquifer system has a diverse surface expression with water-filled sinkholes, karst ponds, karst lakes, and wet prairies. (3) Over the Suwannee Limestone and separated by an unconformity, in turn, lies Plio-Pleistocene age quartz sand-sized material that is well sorted by water and wind-blown transport, with ~85% of these quartz sands between 0.25 and 0.15 mm in diameter (Puri and Vernon, 1959; Rodgers, 2007) (Fig. 2).

Two sea-level shoreline change terraces represent the dominant process that modified the thicknesses of the quartz sand-sized deposits (Healy, 1975). Downward erosion of these quartz sands into the solution cavities, cavern systems, and conduits further shaped the landscape and led to cover-subsidence sinkholes. The karstic erosion is apparent in >30 recognizable karst drainage basins within the Scout Reservation boundaries (Rodgers, 2007).

Willow Sink is one of the largest of the karst lakes on the property (Figs. 1A and 2) and provides a valuable reference data set for the dimensions of karst depressions. The red dots in Fig. 1A show 181 individual depressions mapped in 2007 by B. Rodgers, P.G. when the lake was dry (Fig. 3D). Some depressions are isolated, 30–60 m away from other depressions. The majority lie within semi-circular to irregular clusters ~60 m-wide, with individual depressions ~5–15 m away from one another. Observations made at six locations during exposure of the lakebed noted limestone to be between 0.6 and 2.3 m below the land surface, with a distinct transition to white clay before termination in refusal limestone. In contrast, the depressions augured in another six locations returned clean, white quartz sand to termination depths of about 2.6 m below land surface, where water table collapse prevented further auger advancement.

Between the Plio-Pleistocene surface sands and the underlying limestone lies a white clay textured material (Scott, 2011; Upchurch et al., 2018). This is considered residual clay, resulting from the buried limestone's chemical weathering that is protected from by the overlying sands from mechanical erosion. This physical positioning beneath the quartz sand mantle results in the rounded characteristics of the limestone surface. This pattern is characteristic of rundkarren and can be detected in the ground-penetrating radar imagery of clean quartz sand over shallow limestone.

4. Data acquisition and analysis

GPR and ERT were used for subsurface characterization, while PSInSAR, SfM, and LIDAR were used to monitor subsurface displacement

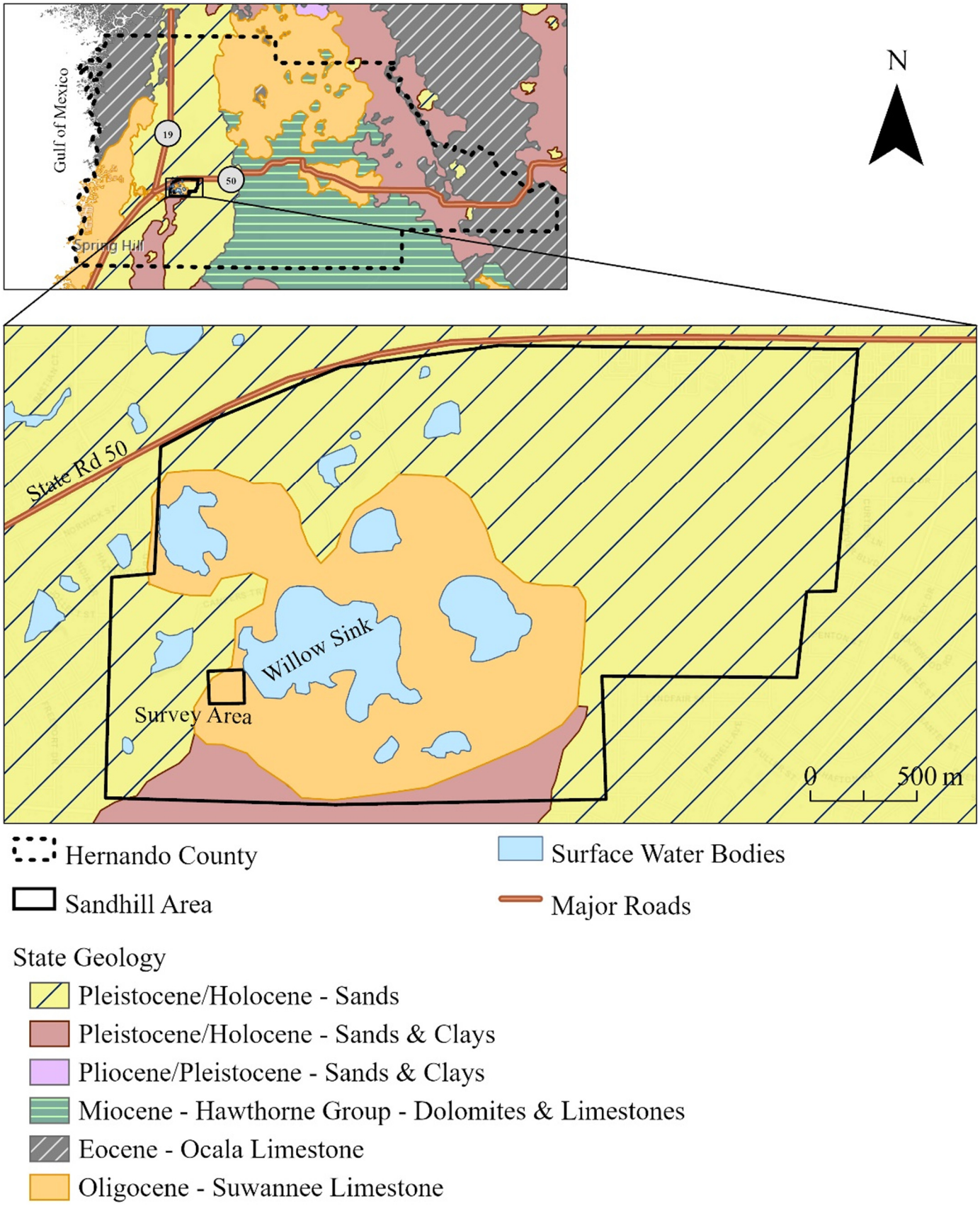

Fig. 2. Geological setting of the Sandhill study area in Hernando County, Florida (from Scott et al., 2001). The Sandhill Reservation and survey area are outlined as in Fig. 1A.

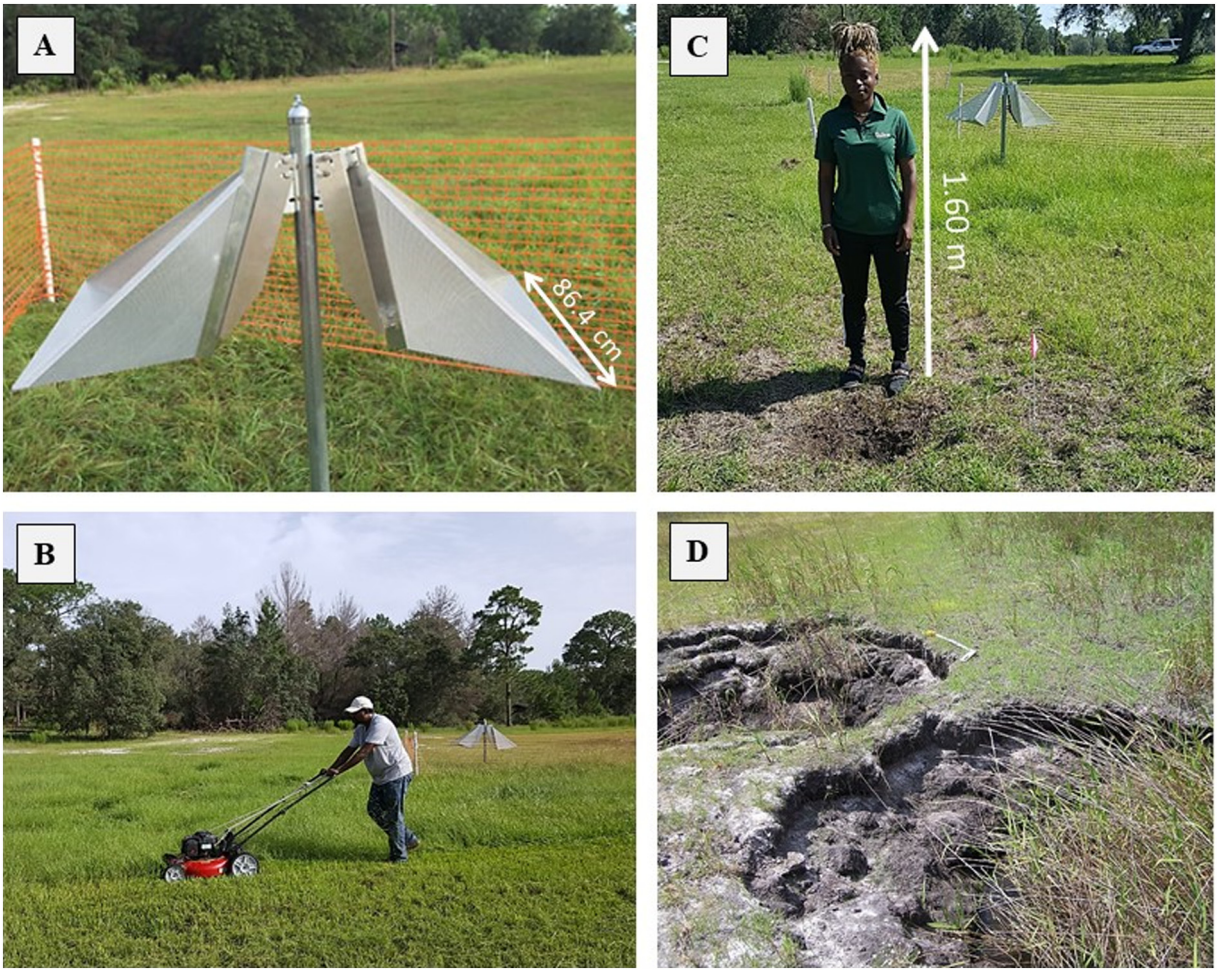

Fig. 3. Field preparation and notable surface features. A: Photo of a trihedral corner reflector mounted on a steel pole (Locations are shown as triangles in Fig. 1). Both reflectors CR-N and CR-S are single steel poles, each with two mounted corner reflectors, where one faces the descending direction and the other the ascending direction of the satellite transmission. B: Preparation of the field where survey areas are mowed to a uniform level to reduce the grass growth's influence on the surface imaging methods. C: Example of surface pits located in the southwest of survey area within penetrometer area A-1. D: Example of observed depressions about 3 m in width found in Willow Sink during the dry season.

over time. The surface penetrometer method was used to measure the strength of the uppermost 0.5 m of topsoil/sand. On 2/11/2015 and 2/15/2015, two drilled borings were completed on the east side of the pool to understand the geological mechanisms influencing the visible subsidence detected at the pool area's eastern corners (Fig. 1C, B-1, and B-2). Geophysical investigations were carried out between 9/18/2015 and 9/20/2015, while PSInSAR data acquisition was between 2015 and 2017. Auger boring analyses were taken at two locations within the study area to acquire direct subsoil information (Fig. 1C). Fig. 1B and C show the locations of all investigations.

Given the temporal distribution of data acquisition, we emphasize that geophysical investigations and auger data represent subsurface structure at the start of PSInSAR data acquisition, while borings completed earlier in the year are mainly used for deeper structural comparison.

4.1. SfM and LiDAR

At other locations in the Sandhill Reservation and near the swimming pool, ground deformation of centimeters or more had been subjectively observed over timescales of months to years. Intermittent shallow pits (Fig. 3C) were observed at the surface within A1 on Fig. 1B. We used Structure from Motion (SfM) photogrammetry of drone images or terrestrial LiDAR scan to resolve subsidence in the grassy field of our study site (Fig. 1B and C). This environment is typical to residential and commercial yards in Florida, and the methods thus potentially hold value for sinkhole investigations. Although these techniques were not successful, we describe them briefly here to present the limits of resolution of these methods. Before applying these techniques, parts of the survey area were mowed to a uniform and consistent level with the same lawnmower (Fig. 3B). LiDAR scans were completed on the dates 25/09/2017, 01/12/2017, and 10/03/2018 (dd/mm/yy) using the FARO Focus3D 330 scanners, which have a nominal 2 mm accuracy. LiDAR datasets were processed with the SCENE software. SfM photogrammetry images were completed by drone flights (at about 100 m) on dates 01/12/2017, 09/03/2018, and 06/07/2018 using ground control points (GCPs) for accurate positioning. Photogrammetry was initially processed using the Agisoft Photoscan Software to create 3D point clouds. The Cloud Compare software was used to align both SfM and LiDAR point clouds using both infrastructures within the survey area and ground control points. Cloud Compare was also used to remove undesirable features such as moving objects or human beings from 3D scans. The point clouds were then converted to DEMs using ArcGIS.

4.2. PSInSAR

Because the reservation is mainly covered by sparse vegetation and loose soils, four metal reflectors were mounted on two poles (referred to as corner reflectors CR-N and CR-S) in the assumed subsiding area in mid-2015 (Fig. 5A). These metal reflectors served as persistent scatterers to continuously provide high amplitude EM backscatter to the SAR vehicle

and subsequently deliver reliable deformation data. SAR images were acquired through the German Aerospace Center from the TerraSAR-X, X-band (3.1 cm wavelength) radar antenna using both the Starring Spotlight and high-resolution spotlight modes (Oliver-Cabrera, 2018; Oliver-Cabrera et al., 2020, 2021). Data acquisition continued from 2015 to late 2017. A total of 69 images were collected for the site location with repeat-pass times of 11 and 22 days and a pixel resolution of 1.1 m × 0.6 m (Oliver-Cabrera, 2018; Oliver-Cabrera et al., 2020, 2021). The Stanford Method for PS (StaMPS) was used to acquire displacement information over time using the PSI technique (Oliver-Cabrera, 2018; Oliver-Cabrera et al., 2020, 2021). The PSInSAR subsidence information for both reflectors is presented as a plot in Fig. 6A, B.

4.3. Penetrometer

Two grids of soil strength penetrometer readings were collected on 02/12, and 04/12/2017 in the areas marked A-1 (20 m by 24 m) and A-2 (20 m by 20 m) (Fig. 1B) and at points collected at a 1 m radius surrounding the northern corner reflector CR-N (Fig. 5C). A handheld soil penetrometer was used to measure shear strength at intervals of 2 m for each survey area. For each penetrometer data point, the operator pushed the instrument's cone tip into the ground at depth intervals of ~0.15 m, where the shear strength is measured at each interval up to a maximum depth of ~0.6 m. The kPa values recorded at each interval were then averaged to represent the shear strength at the point location.

4.4. GPR

Common-offset surveys were completed on Grids 1 and 2 and lines A and D, using a MALA 250 MHz shielded antenna (Fig. 1C). Grids 1 and 2 were collected with survey line separations of 1 m. Grid 1 is approximately 20 m by 80 m, and Grid 2 is 46 m by 50 m. Line D, a 106 m line, runs northwest-southeast within the survey area. Line A also runs northwest-southeast, is approximately 165 m long, and is located along the road outside the subsiding area.

GPR profiles were processed in the Reflex-Win Sandmeier software; version 8.5.8 Processing steps include: (1) *subtract-mean dewow* used to remove low frequencies; (2) one-dimensional *resampling* to a tenth of the sampling window; (3) *time-zero correction* to shift time delay of the first arrival; (4) *resampling* return to original sampling time increment; (5) *time cut* to 160 ns to limit the maximum time window; (6) *background removal* to remove the average from each pro5ile; (7) *Bandpass Butterworth* applies a bandpass filter to remove frequency values lower than 100 MHz and higher than 400 MHz; (8) *gain function* to amplify each trace; (9) *running average* on an average of four traces; (10) *subtracting average* to remove horizontal banding; this step helped to reduce ringing in the signal, but some ringing clearly remains in the final product. (11) *topographic correction* using a best-fit velocity of 0.075 m/ns; (12) *diffraction stack* simple migration with a constant velocity of 0.075 m/ns (13) *correct 3Dtopography* was completed for grids, all referenced to an elevation of 6.70 m, (the lowest surface elevation in the GPR grids); (14) *time-depth* conversion with the same velocity.

Arrival times of two distinctive GPR reflective surfaces referred to as H1 and H2 were picked by following continuous high amplitude returns present in adjacent transects within grids (Fig. 4). Surfaces H1 and H2 appear within fixed depth ranges below the surface (0.2–0.9 m for H1 and 3–5 m for H2) and could thus be tracked based on amplitude, depth, and continuity on other profiles.

For the time slices, the envelope is plotted to emphasize high amplitude returns, and filters were applied for sharpening. All profiles and grids were then plotted using Matlab.

4.5. 2D Electrical Resistivity Tomography (ERT)

The Advanced Geosciences, Inc. SuperSting R8-IP Resistivity meter was used to complete three ERT surveys (Fig. 1C). Each survey had a 52 electrode dipole-dipole Reverse Schlumberger geometry using

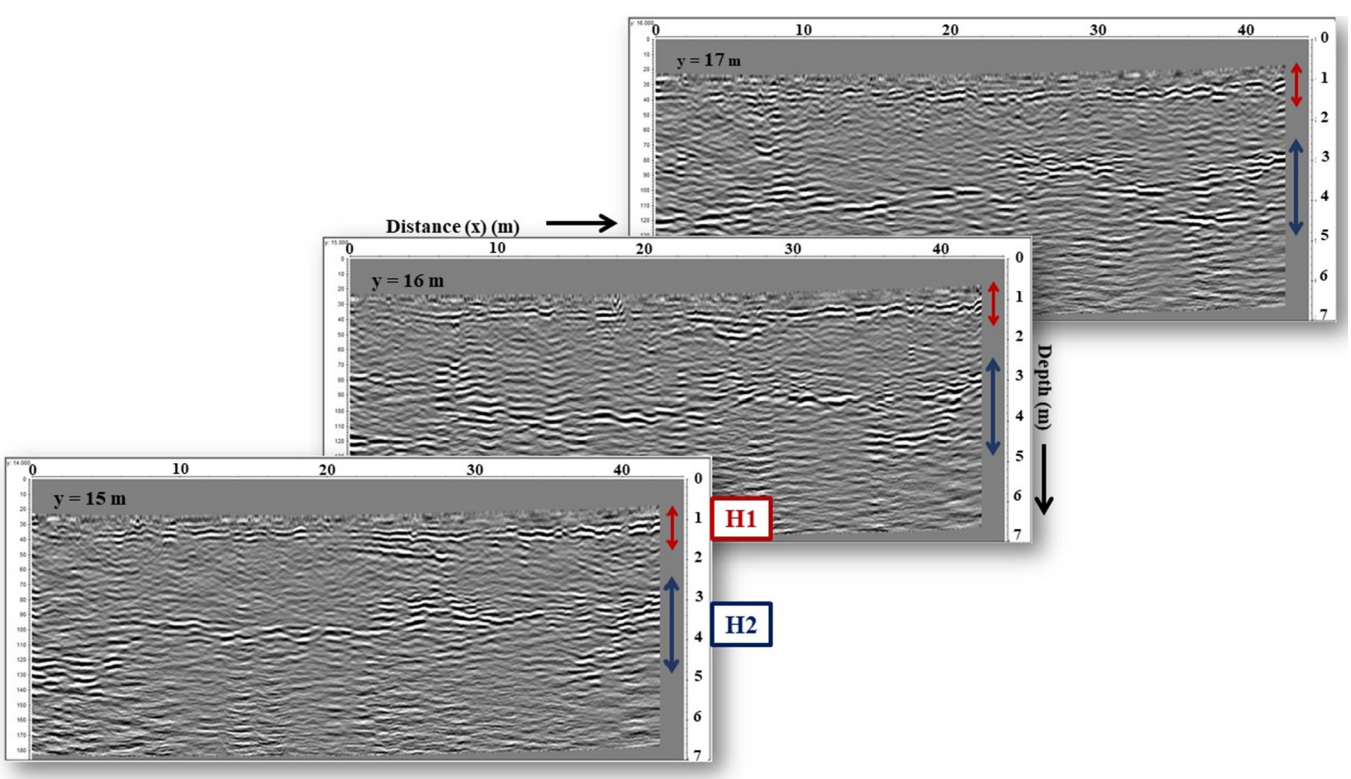

Fig. 4. Example of adjacent processed GPR profiles from Grid 2 (1 m separation). Surfaces H1 and H2 are seen as continuous high-amplitude returns with clear continuity between adjacent profiles. Arrival times are picked based on this continuity. H1 lies 0.2–0.9 m below the surface on all three profiles, while H2 is seen continuously between 3 and 5 m.

standard steel rods. The three profiles consisted of two northwest-southeast lines A and D and one east-west, Line B. ERT Line A is ~153 m long with 3 m electrode spacing. Both Lines D and B are ~102 m long with 2 m electrode spacing. Lines were imported into the Res2DinVx32 ver−3.71 from Geotomo Software for processing. Before processing, topography information was added to each resistivity text file. With the software, outlying points were removed based on statistical deviations from model fits, and the default least-squares inversion was used. After processing in Res2DinVx32, each inverted profile was plotted using Matlab.

5. Results

5.1. Surface maps

The 1 m DEM acquired from the National Elevation Dataset (National Elevation Dataset, 2011) shows a ~60 m-diameter irregular depression within the survey site (Fig. 5A). Our tests of whether sinkhole-scale subsidence within this grassy area could be detected over timescales of months or years by ground-based methods were unfortunately unsuccessful. The apparent elevation changes derived from sequential surveys with SfM were well beyond a few centimeters (from −0.4 to +1.2 m), demonstrating that errors in differencing SfM images in this grassy field were too large to make the method useful.

Elevation differences from sequential terrestrial LiDAR scans were less than 2 cm in the consistently mowed areas, which appear as square and rectangular shapes surrounding the reflectors in the difference image (Fig. 5B). Thus terrestrial LiDAR in mowed grassy fields could be used to detect ~>2 cm or more of ground motion, but as described further below, this is an order of magnitude larger than what was measured at the two reflector locations. Benito-Calvo et al. (2018) similarly reported that compared to high-precision leveling, LiDAR failed to capture the known subcentimeter (<0.6–1 cm) change on the margins of a subsiding sinkhole. The only semi-circular feature (as might be expected for sinkhole deformation) in the time-lapse imagery of 'clean' mowed areas is a ~1 m diameter ring of apparent uplift, ~5 m NNW of CR-N in Fig. 5B.

5.2. Penetrometer grids

The overall mean of all penetrometer measurements is ~1860 kPa (Fig. 5C). The value plotted at each location on the grid represents the average value at all depths recorded at that site. The higher shear strength values may be related to the presence of organic soils, which can become solid when dry. In contrast, note the lower average measurements (<1790 kPa) in Grid A-1 typically reflect the presence of isolated weak zones (<15 cm thick within the uppermost 60 cm) with kPa values of only 7–70 kPa. These zones appear to include voids below the grass mat, suggesting that sediment is raveling downward or along an incline away from these areas. These smaller low-kPa zones, which plot as greens in Grid A-1, are not circular but show a slight north-south elongation. A notable zone of higher compaction (>2200 kPa) also exists between CR-S and CR-N. In penetrometer grid A-2 (Fig. 5C), high kPa values (>2200 kPa) correlate with a vehicle path and exposed surface soils. In contrast, the southern margin of A-2 with low kPa values (<1860 kPa) corresponds to grassy soils that appear superficially similar to those with mid-range kPa values on the southern edge of grid A-1.

5.3. PSInSAR reflectors

Fig. 6 shows that vertical motion in the grassy field topographic low could not be resolved from the InSAR data before the installation of the corner reflectors (blue-gray versus dark blue points). After the corner reflector installation in fall 2015, the time series of the reflectors show millimeter-scale changes in elevation over the acquisition period. Subsidence rates differ for the two reflectors. Although reflector CR-S is roughly centered at the low within the ~60 m-diameter, ~1.5 m-depth quasi-circular depression (Fig. 5A) is not demonstrably subsiding: the apparent rate is −0.13 ± 0.15 mm/yr. In contrast, CR-N, which sits higher on the flank of the depression, is subsiding at −1.03 ± 0.17

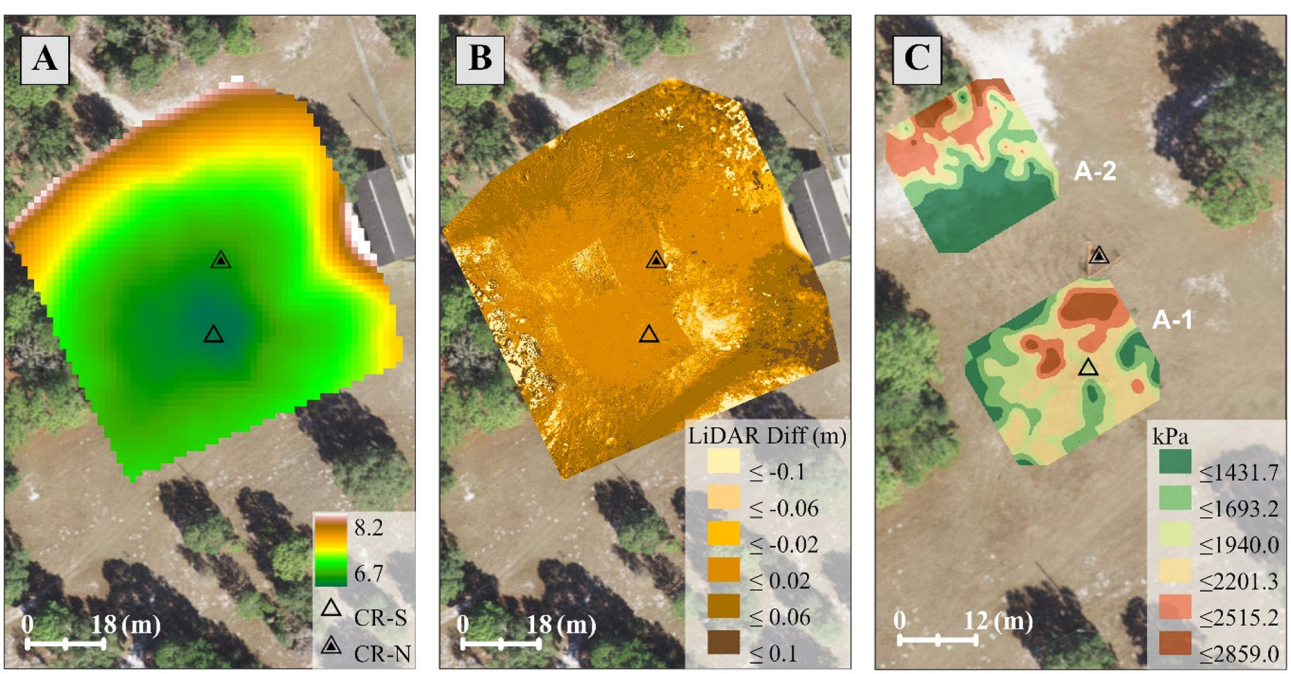

Fig. 5. A: 1 m DEM of area, acquired from the National Elevation Dataset and collected 2007. B: Difference between 3rd and 1st LiDAR dataset collected between the dates 25/09/2017 and 10/03/2018. Tan rectangular areas (difference less than ±0.02 m) are where the grass was consistently mown C: Contour of average surface penetrometer data collected at 1-m intervals in 01/12/2017 using a handheld penetrometer, units are in kPA. Note the scale differences: maps panels A and B are 1:900 while panel C is 1:600. Around reflector CR-N penetrometer readings were collected 1 m North, South, West, and East of its location.

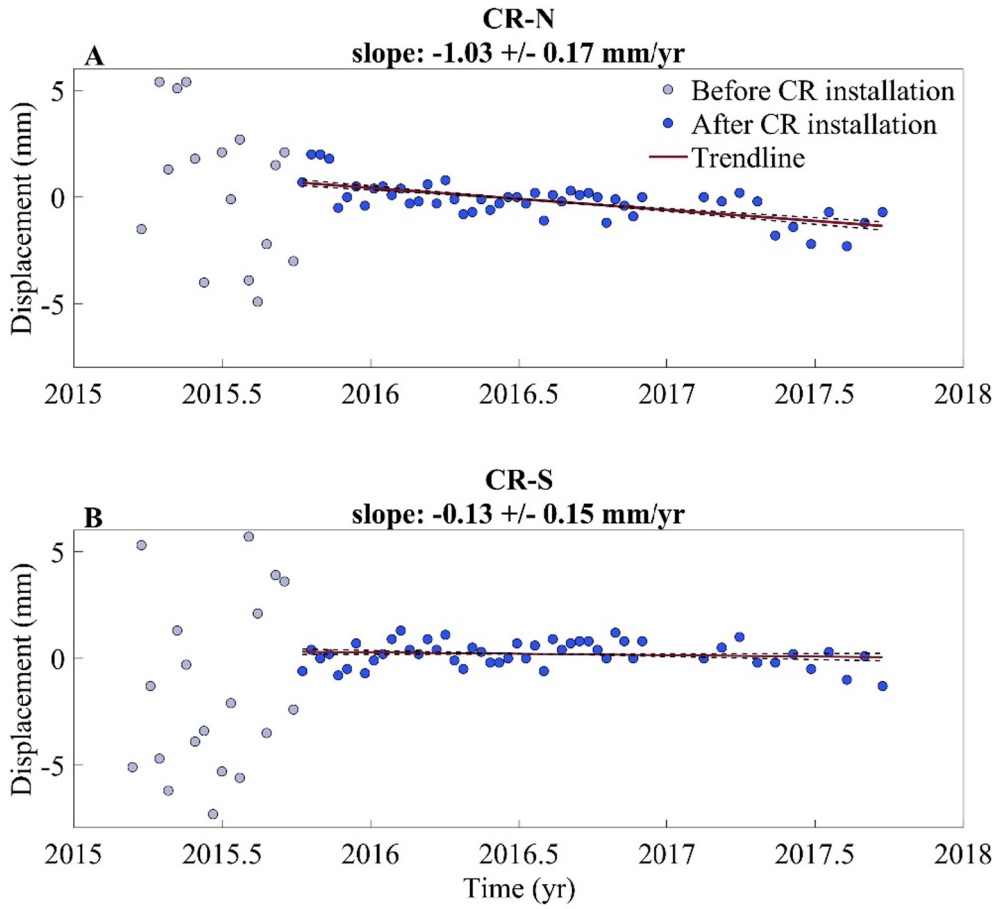

Fig. 6. InSAR-derived displacements at the corner reflectors over two years. Locations are shown in Fig. 1C. A: displacement for the north corner reflector. B: displacement for the south corner reflector. RMSE values before and after installation are 3.29/0.64 mm and 3.86/0.58 mm for CR-N and CR-S, respectively.

mm/yr. The quoted rate uncertainties (±0.15 mm/yr and ±0.17 mm/yr) are based on the assumption of white (uncorrelated) noise and thus may under-estimate the true uncertainty (Mao et al., 1999).

5.4. ERT and GPR profiles

ERT profiles extend to a depth of 35 m in Profile A (Fig. 7) and ~25 m in Profiles B and D (Figs. 8–9). GPR profiles to maximum depths of ~8 m. The previously described two distinctive GPR reflective horizons are identified on the GPR profiles and labeled as H1 and H2 on both the GPR and resistivity images (Figs. 7–9). The shallower H1 horizon consistently appears close to the measured depth of the water table. The deeper horizon H2 correlates with the presence of a more clay-rich layer underlying cleaner sands (coring B-1; Fig. 7).

Resistivity values in the survey area decrease with depth and range from 5 to 20,000 Ω-m with the selected inversion parameter. All profiles show a laterally continuous high resistivity zone (5000–20,000 Ω-m) in the first meter below the surface; this corresponds to the drier sands close to the surface as seen in the auger and boring classifications (Figs. 1C and 7). The water table's location at approximately 1–2 m depth below the surface is evident in each profile (Figs. 7, 8 and 9). It appears as a distinctive gradient from higher resistivities above to lower resistivities below. Layer H2 coincides with lower resistivity values of 500–1000 Ω-m; its hummocky shape also loosely correlates with the sinuous pattern of the gradients in each resistivity profile.

Profile A has a distinct central low resistivity zone below about 1 m depth (Fig. 7). This low resistivity area has the form of a 2D funnel and widens deeper into the subsurface. Gaps within the plotted GPR surface H2 correlate with this low resistivity area and other lateral variations in the resistivity profile (~−40 m and +20–40 m). We note both corings B1 and B2 encountered limestone at their base, but at dramatically different depths (~10 m versus ~20 m), and B2 shows a ~3 m long section of void or loose sand.

The combined Profile A data indicate that the low-resistivity zone represents a conduit or fracture extending to at least 20 m deep, breaching the H2 layer. Overall the data imply dramatic variations in depth to limestone over 10 m distance, even below a gentle topographic gradient.

Profiles B and D (Figs. 8 and 9) pass within ~15 m of the ~60-m diameter topographic low west of the swimming pool (Fig. 1C) and show less variability below the water table than Profile A. Both profiles show lower resistivities in the uppermost 1–2 m within the topographic depression, suggesting surface sands are wetter in the topographic low and dryer higher on the flanks. The H2 horizon depths roughly follow resistivity contours, as expected if the GPR reflection corresponds to the top of a more conductive layer. At some locations, abrupt changes in the depth to H2 appear to coincide with lateral gradients at depth in the resistivity profiles (e.g., ~48–50 m on Profile B), but at others, they do not (~+20 m on Profile D).

5.5. GPR time slices and reflector elevation plots

Time slices for the 3D GPR grids acquired around the central depression of the study site are shown in Fig. 10. We note that depths reported for each slice are below a fixed elevation of 6.70 m (the lowest point within local topographic low, see DEM, Fig. 5A) to permit the reader

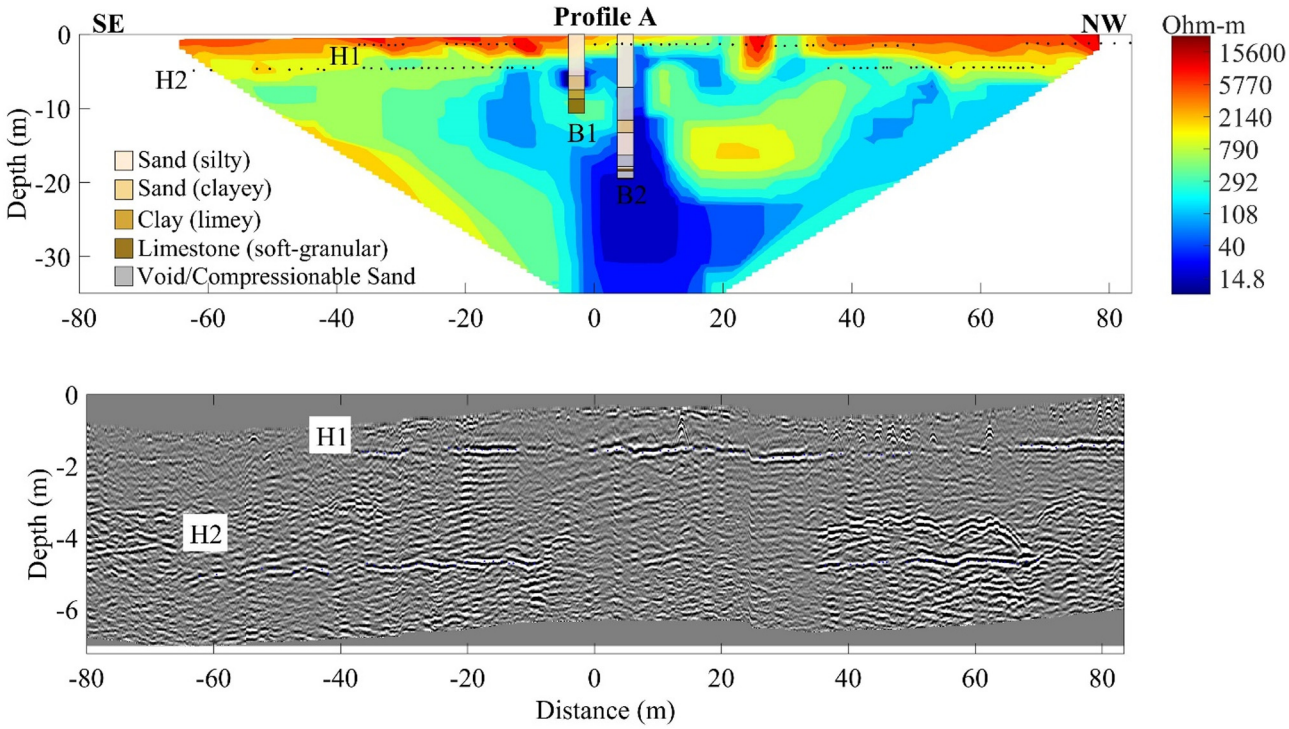

Fig. 7. Top: 153-m long ERT line A with borehole data on the east side of the swimming pool (Fig. 1C). The dotted lines at ~1 m and ~5 m below the surface show the H1 and H2 horizons picks, respectively, along the GPR profile at the exact location. H1 is interpreted as an alteration surface within the sands, close to the water table. H2 is interpreted as the top of clayey sands or clays that drape the underlying limestone. Boreholes B1 and B2, although only 10 m apart, show very different depths to limestone (~10 m and 20 m, respectively). Bottom: GPR profile A with picks of reflecting horizons H1 and H2 in blue.

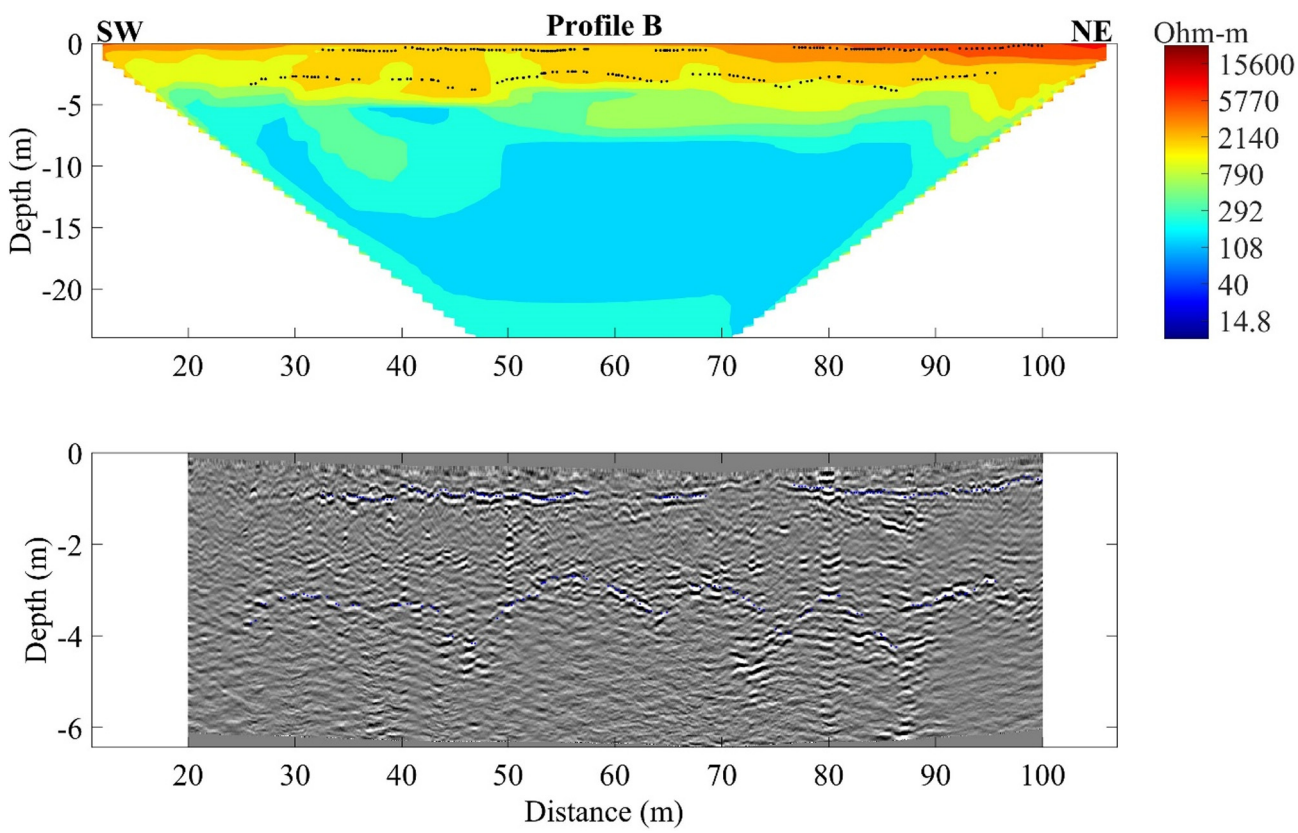

Fig. 8. Top: Resistivity profile B within GPR Grid 1 along the southeastern flank of the topographic low. Location is shown in Fig. 1C—all labeling and notation, and interpretation as in Fig. 7. The black dots plotted on the figure are picks from strong GPR reflecting horizons H1 and H2 taken along the GPR line closest to line B (Line 10 in Grid 1). Bottom: GPR profile along the same path; same picks shown in blue.

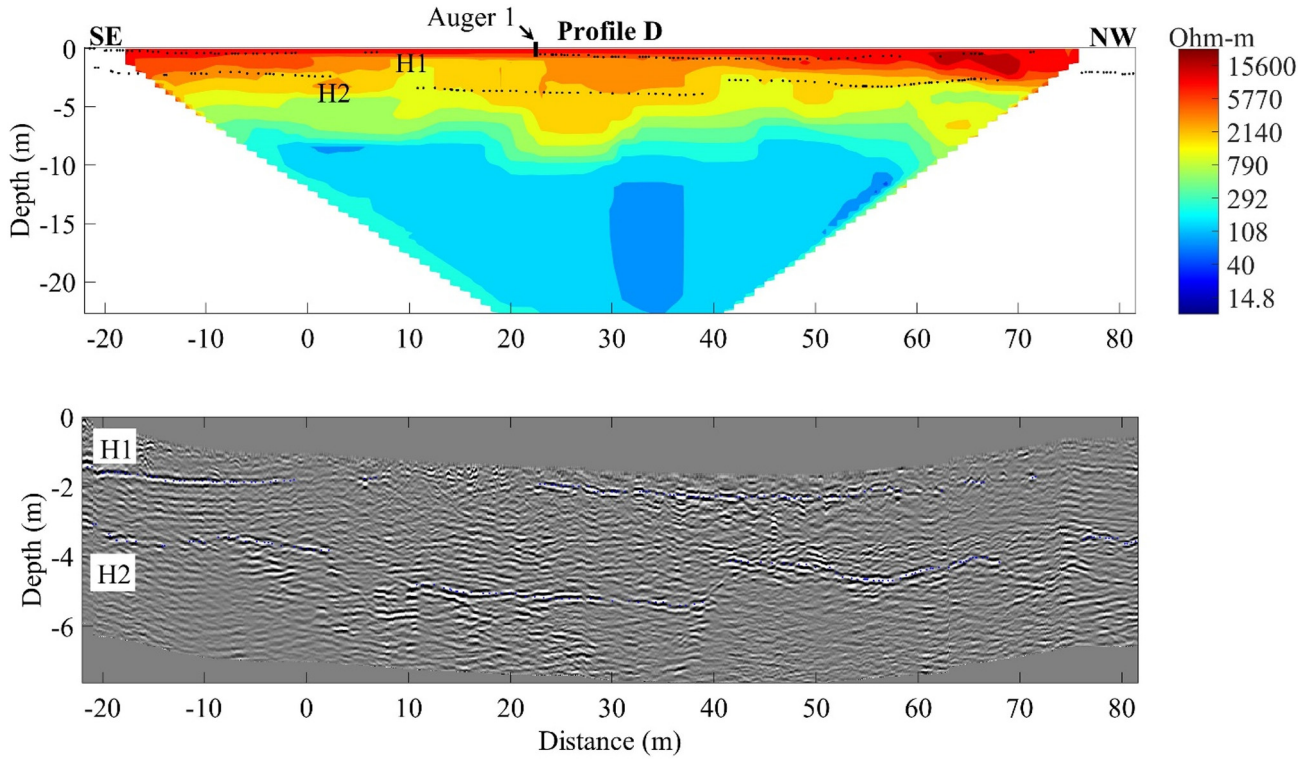

Fig. 9. Top: Resistivity Profile D along the southwestern flank of the topographic low. The location is shown in Fig. 1C: all labeling and notation, and interpretation as in Figs. 7 and 8. The black dots plotted on the figure are picks from strong GPR reflecting horizons H1 and H2. Bottom: GPR profile along the same path; same picks shown in blue.

to visualize an undistorted data cube. Time slices 7–20 ns for the combined grid show a quasi-circular feature that corresponds to horizon H1 in Figs. 7–9. The depth of this H1 horizon below the ground surface is contoured in Fig. 11A to highlight differences between surface and reflector elevation. The reader is cautioned that the horizon is absent or ambiguous in the parts of the grid without black dots, including much of the central part of the depression around CR-S. Overall this H1 horizon appears flatter away from the edges of the topographic depression (Fig. 11A; also see edges of GPR, Figs. 8 and 9). H1 has a central tilted conical depression, roughly centered around and similar to the current topographic low, tilted down approximately 10–15 cm and broader on the west relative to the east (Fig. 10, time slices 7.95–20 and Fig. 11A).

Deeper GPR time slices, 72–90 ns (2.7–3.4 m depth below 6.70 m elevation), show more patchy and irregular zones of high amplitude reflections (Fig. 10). Below ~4.3 m depth (below 6.70 m), the strongest reflections are consistently concentrated in a ~20 m-wide zone to the southeast of the reflectors. These deeper slices (>72 ns) correlate with the plotted horizon H2 (Fig. 11B). H2 geometry is dramatically different from H1, with more pronounced (3 m) changes in elevation over much shorter distances (~2–10 m). H2 shows a low trough in the same ~20 m-wide zone southeast of the CR's, although similar depths are observed elsewhere in the grid. GPR picks of H2 in this central trough are discontinuous but more extensive through the zone than the shallower H1 horizon (Fig. 11).

6. Discussion

6.1. GPR horizons H1 and H2

Our interpretation of the asymmetrical conical H1 horizon (Figs. 7–10, 11a) is that it represents a sandy unit with some alteration that developed because of the water table's influence for extended periods. The water table is expected to follow a muted version of the surface topography. If H1 formed at a typical elevation of the water table (which does vary with rainfall), that would explain why H1 is flatter than the land surface on the edges of the depression. The depression in the H1 horizon (about 0.6 m from edge to deepest part of zone imaged in Fig. 11A) presumably then reflects either ongoing "conical" subsidence since its formation at a uniform elevation or the presence of a water table low in the topographic low during the period of formation or both. It effectively outlines the opening of an inferred conduit. The gaps in H1 in the ~10 m-zone around the topographic low suggest this horizon has been breached, presumably because of sediments raveling into underlying voids.

The 2–5 m deep, more undulating H2 GPR horizon (Figs. 7–10, 11B) is interpreted as a contact between more resistive sandy surficial sediments and more conductive silty or clayey sands or the clays that form the residual weathering product of the underlying limestone, as described in Section 3. This interpretation is based on the correlation between H2 depth and coring B1 (Fig. 7) and the loose correlation of H2 depth with a transition between shallower higher resistivities deeper lower resistivities (Figs. 7–10).

6.2. Covered karst structure and processes

As in Gutiérrez et al. (2011) and Carbonel et al. (2015), GPR provided centimeter to tens of meter scale detail on geometry of the karst cover sediments. The combined topographic, coring, penetrometer, GPR, and ERT data show two distinct spatial scales of deformation. The ~60 m topographic depression of the study site (Fig. 5A) is similar in scale to the major (60 cm vertical) H1 horizon depression and the diameter of the clusters of depressions, both ring-like and irregular, observed at nearby Willow Sink (Figs. 1A and 3D). Within these ~60 m-diameter features are perturbations with ~5–20 m horizontal length scales. These smaller-scale features include the spacing between individual depressions in Willow Sink clusters, the scale of voids/low kPa zones detected in the uppermost 60 cm sands (Fig. 5C), and the ~3 m vertical perturbations in the depths to the H2 horizon (Fig. 11B).

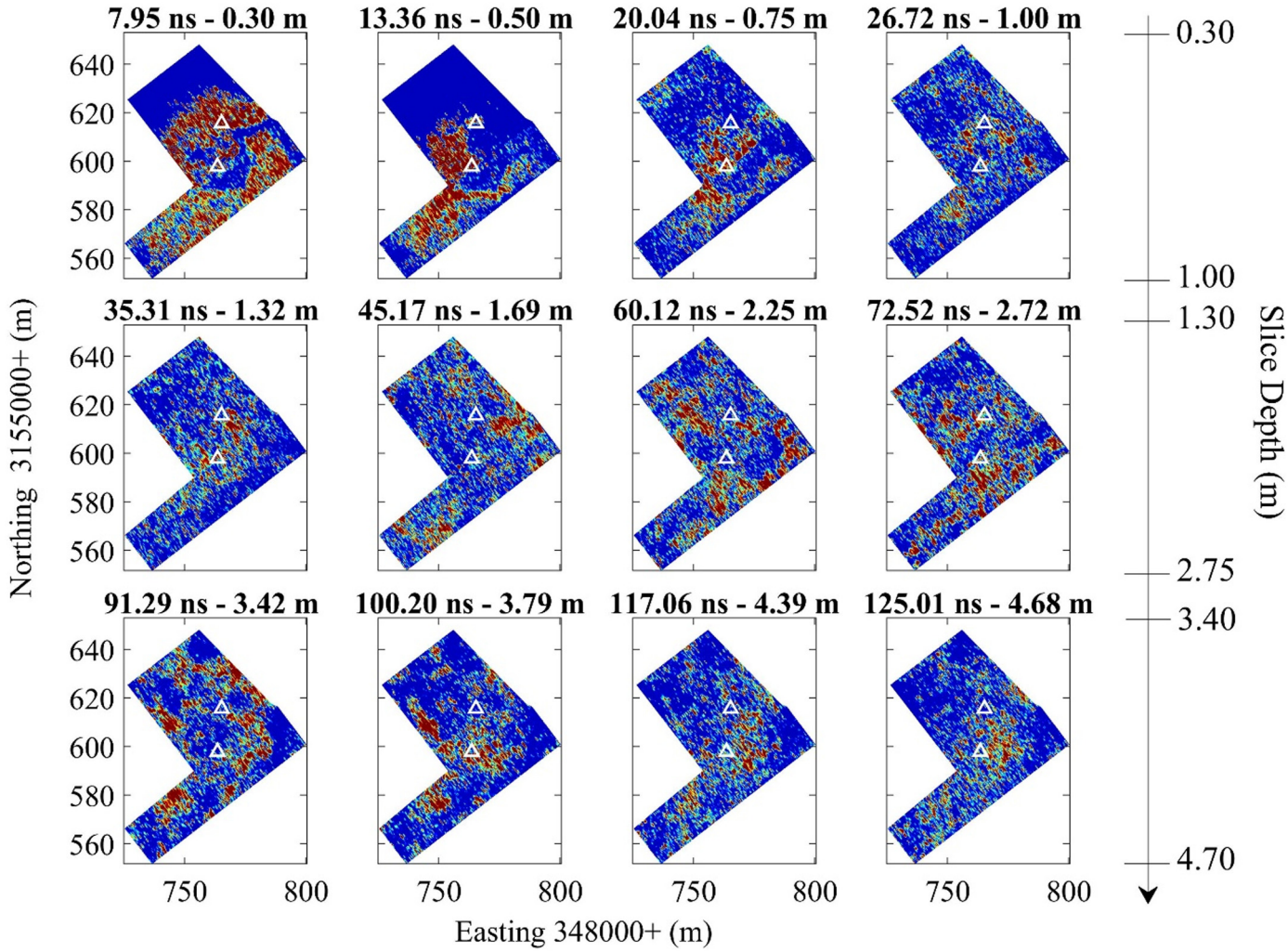

Fig. 10. Time (elevation) slices of elevation-corrected and 3-D migrated GPR Grids 1 and 2. Red = high amplitude return; blue = low-amplitude. Depths are given below the reference elevation of 6.70 m, i.e., below the topographic low in the survey area. The triangles mark the location of the north and south reflectors, CR-N and CR-S, respectively. The southern reflector lies near the topographic low.

In the case of H1, we posit that this return is predominantly from a layering within the surface sediments that lie close to the water table. This is because (a) this horizon has similar gaps in continuity in neighboring GPR profiles, especially within the areas surrounding CR-S in the local topographic low (Fig. 11A), and (b) GPR studies in similar sandy settings have shown that the water table does not appear clearly when using antenna frequencies higher than 100 MHz (Kruse et al., 2006; Downs, 2017), presumably because of a capillary fringe rather than a step-function change in water content with depth, and (c) processes associated with the water table itself may have influenced the sediments, generating porosity or other contrasts that cause or enhance the radar reflection. The deeper horizon (H2), interpreted as top of a clay-rich layer, appears similar to clay-rich layers observed elsewhere in the covered karst of west-central Florida, where such layers have been found to generally drape the shape of the top of the underlying limestone (e.g., Tihansky, 1999; Kruse et al., 2006; Bumpus and Kruse, 2014). (Stratigraphic contacts commonly produce GPR reflections from well below the water table (e.g., McClellan et al., 2017; Wright et al., 2018).

The profiles B and D (Figs. 8 and 9) results suggest that the relationship between the H2 layer and underlying structure of clayey/silty sediments and limestone may be complex and/or that these structures are so three-dimensional that variability is not resolved in a 2D resistivity profile. Such complexity is observed in the 3D plots of GPR depth described in Figs. 10 and 11.

These observations are combined schematically in Fig. 12. This figure illustrates the notable disconnect between the surface topography (~60 m-scale) and numerous smaller ~5–20 m-scale depressions in the clayey sand or clays that drape the top of limestone (Fig. 11B). We hypothesize that this disconnect occurs because of the inconsistent deformational behavior of the karst cover materials. On the surface, the grass mat with its intertwined roots has sufficient strength to smooth over shallow voids/high porosity zones that form in the underlying sands as the sands migrate downward, eventually into interstices within the limestone. The lower sands must migrate laterally and downward into the deepest H2 depressions. However, the H1 horizon within the sands varies generally smoothly over the 60-m scale of the depression, with only smaller-scale local perturbations and breaches. The exception to this is the irregular ~10–15 m diameter zone centered around the topographic low, where the H1 layer is mostly absent, suggesting a concentrated loss of stratigraphic continuity.

The GPR data suggest temporal as well as spatial complexities. Significant depressions exist in the H2 horizon on the flanks of the topographic low (Fig. 11B). These may overlie voids that are plugged or filled long before the activity of the central topographic low. Alternatively, shallow cohesive organic sediments and the grass mat may have inhibited local surface deformation, drawing sands from wider lateral zones. An exception would be the surface pits (Fig. 3C). The one circular "uplift" observed in the sequential terrestrial LiDAR scans could be such a pit that was filled through erosion over the duration of the

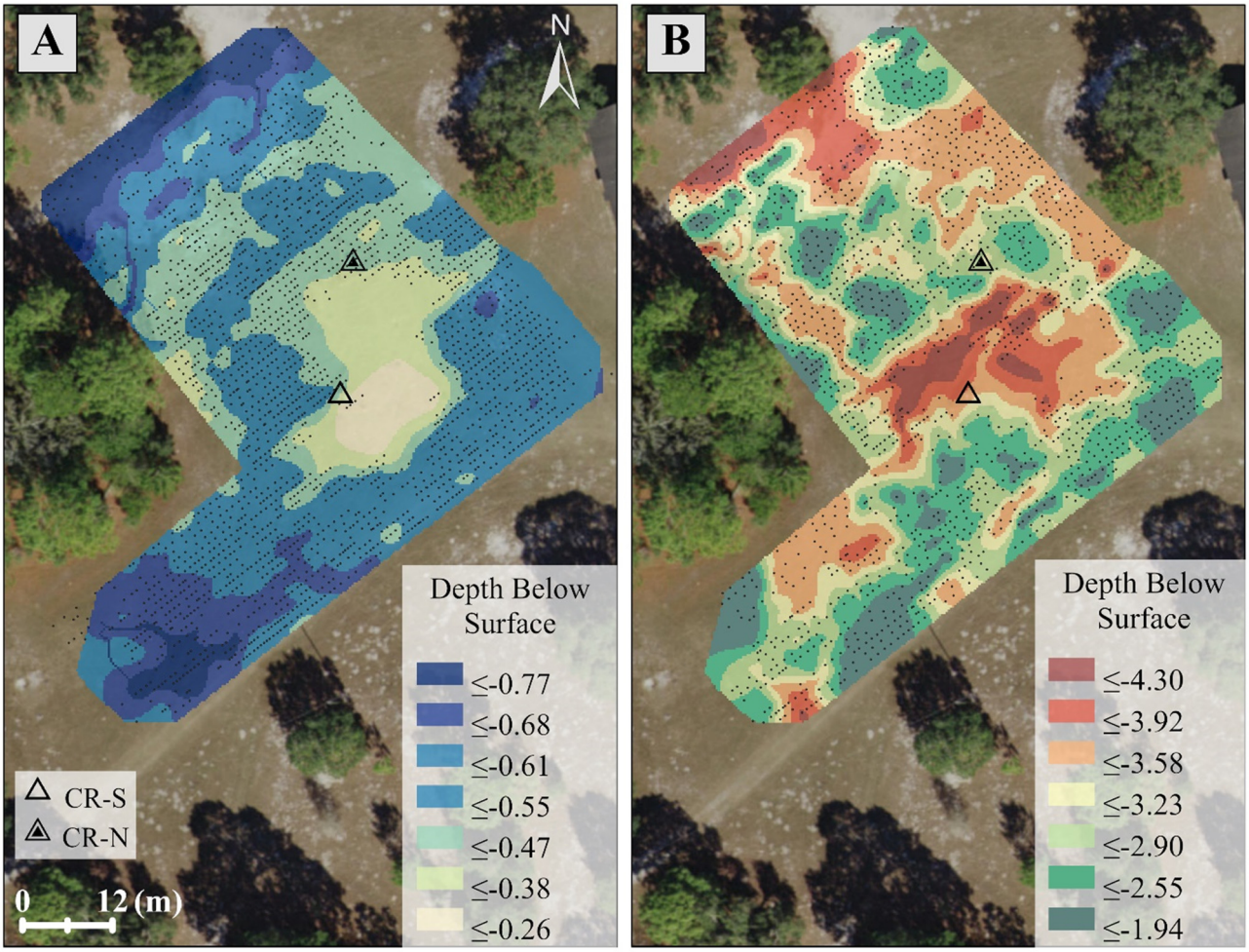

Fig. 11. Depth contours of the two strong GPR reflection horizons derived from Grids 1 and 2. The black dots represent pick locations along GPR lines within the grids. Contours are plotted as depth below the surface. These horizons are also shown in Figs. 7–9. The alignment of some color contours with the NE-SW GPR line direction is a result of slight differences between neighboring profiles of the phase of the high amplitude return selected for the arrival time pick and of the time-zero correction on each profile. CR-S and CR-N are corner reflectors. A: Horizon H1. B: Horizon H2.

images. (Other pit-like features were captured in individual LiDAR surveys, but their evolution overtime was not resolvEd.)

Interestingly, the lower clayey sands or clays of the H2 horizon inferred to drape the underlying limestone show greater continuity across the central topographic low where the H1 layer is breached. This suggests that cleaner sands from the surface make their way through gaps in the more coherent clayey horizon into underlying voids.

Additional evidence for the complexity in deformation patterns is that the cracking in the swimming pool and the corner of the pool house (Fig. 1B), clear signs of subsidence, are found on a topographic high that separates the study site low from Willow Sink. Profile A (Fig. 7), which runs along this topographic high, shows more pronounced variability in the resistivity signatures at depth than Profiles B and D (Figs. 8 and 9), suggesting lower porosity or void space may be currently present there.

The combined observations suggest that deformation at the Sandhill Reservation is much more complicated in both time and space than the textbook models for sinkhole deformation. To generate our Fig. 12 schematic, we combined modified versions of Tihansky's (1999) simple model of a single central conduit beneath a topographic low, into which overlying sand ravels or pipes or suffoses. Each of the smaller sinkholes forming the larger structure may be at a different stage of development. The overlying topography may reflect primarily past rather than present activity.

6.3. Study limitations and possible future work

The surface analysis could be improved by extending the time window of LiDAR and SfM surveys and applying precision analysis techniques (James et al., 2017). GPR investigations could be improved using lower frequency antennas to resolve deeper structures; Carbonel et al. (2015) used 100 MHz shielded and 50 MHz unshielded. Lower frequencies should limit wave attenuation at the center of the topographic low, albeit with reduced spatial resolution.

The advantages of more direct ground-truthing are apparent in other studies. Boreholes in similar work provide detailed information on the subsurface stratigraphy (Gutiérrez et al., 2008), although the distance over which borehole data is relevant is highly uncertain in karst terranes (Gutiérrez et al., 2008). Similar studies use trenching to avoid this limitation (Gutiérrez et al., 2011; Carbonel et al., 2015; Sevil et al., 2017; Fabregat et al., 2019); trenching is used to give in-depth geochronological information about past sinkhole collapses. However, trenching is undesirable on the Sandhill Reservation because of its invasive nature. Auger corings were completed simultaneously with geophysical studies and provided information about the water table depth (Fig. 1C). We note that borings in this study were completed before geophysical investigations and thus are not an entirely accurate representation of the subsurface at the time of data acquisition (Fig. 7).

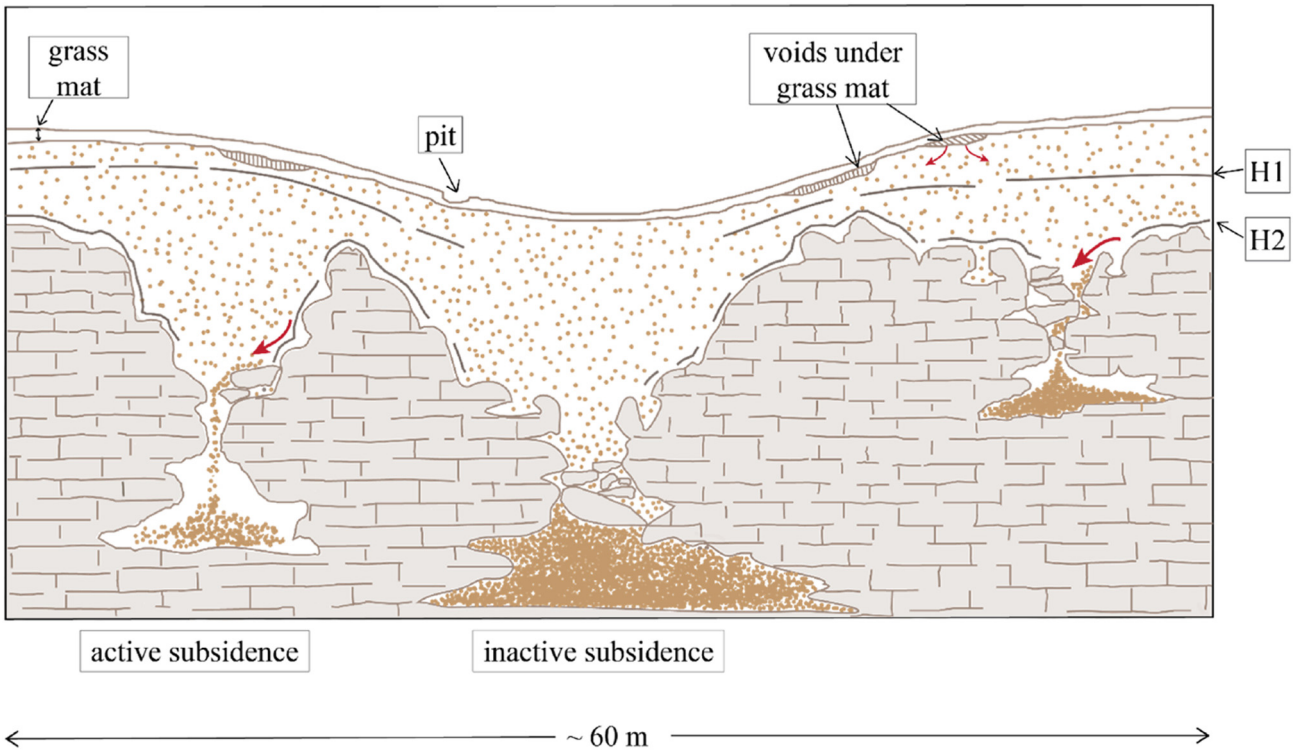

Fig. 12. Schematic of the possible small-scale subsurface processes resulting in the various features imaged and monitored within the survey area, not drawn to scale. H1 and H2 horizons represent schematically the GPR horizons contoured in Fig. 11A and B, respectively. We interpret H1 as an alteration horizon within the sands that formed near the water table and H2 as the undulating top of a clay-rich horizon associated with irregular limestone dissolution and weathering. Spacing between the depressions in H2 is ~5–20 m.

6.4. InSAR and surface data

The PSInSAR data clearly illustrate that the surface topography is incongruent with current deformation. The flank of the depression (reflector CR-N) is subsiding (over two years) demonstrably faster than the center of the depression (reflector CR-S). Furthermore, CR-N is mounted on the flank of a continuous local high in the H2 horizon, so this cannot reflect a simple downward vertical flux into a limestone void. PSInSAR data interpretation is limited by spatial coverage; additional corner reflectors would improve our understanding of the widespread smaller-scale deformation occurring throughout the survey area. Spatial coverage was expected to be extended with the use of LiDAR and SFM-derived surface subsidence data. However, the uncertainties in both LiDAR and SfM datasets were larger than the ground motions outside of pits. The surface analysis could be improved by extending LiDAR and SfM surveys and applying precision analysis techniques (James et al., 2017). Lengthening the monitoring period would allow each technique to capture the millimeter/year changes detected by the PSInSAR method. Benito-Calvo et al. (2018) also suggest complementing LiDAR surveys with high precision leveling to improve DEM accuracy required from the scans.

Oliver-Cabrera et al.'s (2021) larger survey of clusters of persistent scatterers in developed parts of west-central Florida reliably identified sinkhole-related subsidence occurring at rates of 3–5 mm/yr. We note that the installation of corner reflectors for this study permitted slower rates of motion to be reliably determined, among the slowest available from InSAR analysis (e.g., Ferretti et al., 2007). Our results suggest CR installation could be an effective method for monitoring sites of high-risk motions in vegetated terrains.

7. Conclusions

The Sandhill Reservation is a relatively untouched site in a developed urban setting, surrounded by neighborhoods with significant residential sinkhole damage claims. It thus provides an ideal setting for imaging structures and subsidence within the covered karst. Analysis of surface topography, corings, penetrometer data, GPR and ERT profiles, and InSAR-detected subsidence at two reflectors shows that:

- Two scales of features exist. A topographic depression and clusters of small depressions occur with diameters of ~60 m. Underlying undulations in the top of limestone and spacings between individual depressions are smaller, ~5–20 m.
- On the ~60 m-topographic depression, a point on the flank (CR-N) has subsided at ~1 mm/yr over three years, while the central low (CR-S) is stable within measurement error (±0.15 mm/yr).

We hypothesize that:

- The surface topography diverges from the underlying karst complexity because of the strength of the grassy mat and shallow organic layers. Underlying surface sands flow both laterally and downwards into the complex limestone and leave behind the shallow high-porosity zones or voids detected with penetrometer tests.
- Surface subsidence rates are likely complex in time and space as voids open and fill in the underlying limestone, and cover sands migrate.

Finally, we note that resolving subsidence rates is much more difficult in the grassy and vegetated Florida karst than in arid settings. Subsidence within the grassy field could not be detected before the installation of corner reflectors. Even with consistent lawn mowing, SfM from drone images and terrestrial LiDAR were not useful to this study. Thus InSAR monitoring of Florida sinkhole-related subsidence is best done through persistent scatterer analysis from buildings and roads (Oliver-Cabrera et al. (2021)) or through corner reflector installation at sites of interest.

Declaration of competing interest

The authors declare that they have no known competing financial interests or personal relationships that could have appeared to influence the work reported in this paper.

Acknowledgments

We thank Garrett Speed and Jorge Gonzalez Garcia of the USF Digital Heritage and Humanities Collections for terrestrial LiDAR and SfM data acquisition, the 2015 Principles of Applied Geophysics class at USF for their assistance in data acquisition, and Geoview, Inc. for the loan of geophysical equipment. We thank the Boy Scouts of America for their generous access to the Sandhill Reservation for surveys and reflector installation and UNAVCO for installing the reflectors. This work was supported by NSF EAR-1620617, and EAR-1713420, and an FG-LSAMP Bridge to the Doctorate Fellowship awarded to T. Robinson, funded through NSF HRD-1612347.

References

Al-Halbouni, D., Holohan, E.P., Saberi, L., Alrshdan, H., Sawarieh, A., Closson, D., Walter, T.R., Dahm, T., 2017. Sinkholes, subsidence, and subrosion on the eastern shore of the Dead Sea as revealed by a close-range photogrammetric survey. Geomorphology 285, 305–324. https://doi.org/10.1016/j.geomorph.2017.02.006.

Al-Kouri, O., Al-Fugara, A., Al-Rawashdeh, S., Sadoun, B., Sadoun, B., Pradhan, B., 2013. Geospatial modeling for sinkholes hazard map based on GIS & RS data. J. Geogr. Inf. Syst. 2013, 584–592. https://doi.org/10.4236/jgis.2013.56055.

Andrade-Gómez, L., Rebolledo-Vieyra, M., Andrade, J.L., López, P.Z., Estrada-Contreras, J., 2019. Karstic aquifer structure from geoelectrical modeling in the Ring of Sinkholes, Mexico. Hydrogeol. J. 27, 2365–2376. https://doi.org/10.1007/s10040-019-02016-w.

Aurit, M.D., Peterson, R.O., Blanford, J.I., 2013. A GIS analysis of the relationship between sinkholes, dry-well complaints, and groundwater pumping for frost-freeze protection of winter strawberry production in Florida. PLoS One 8, e53832. https://doi.org/10.1371/journal.pone.0053832.

Baer, G., Schattner, U., Wachs, D., Sandwell, D.T., Wdowinski, S., Frydman, S., 2002. The lowest place on Earth is subsiding—an InSAR (interferometric synthetic aperture radar) perspective. Geol. Soc. Am. Bull. 114, 12–23. https://doi.org/10.1130/0016-7606(2002)114<0012:tlpoei>2.0.co;2.

Baer, G., Magen, Y., Nof, R.N., Raz, E., Lyakhovsky, V., Shalev, E., 2018. InSAR measurements and viscoelastic modeling of sinkhole precursory subsidence: implications for sinkhole formation, early warning, and sediment properties. J. Geophys. Res. Earth Surf. 123, 678–693. https://doi.org/10.1002/2017jf004594.

Bell, J.W., Amelung, F., Ferretti, A., Bianchi, M., Novali, F., 2008. Permanent scatterer InSAR reveals seasonal and long-term aquifer-system response to groundwater pumping and artificial recharge. Water Resour. Res. 44. https://doi.org/10.1029/2007wr006152.

Benito-Calvo, A., Gutiérrez, F., Martínez-Fernández, A., Carbonel, D., Karampaglidis, T., Desir, G., Sevil, J., Guerrero, J., Fabregat, I., García-Arnay, Á., 2018. 4D monitoring of active sinkholes with a terrestrial laser scanner (TLS): a case study in the evaporite karst of the Ebro Valley, NE Spain. Remote Sens. 10, 571. https://doi.org/10.3390/rs10040571.

Breithaupt, Charles, 2016. Cave Detection Using Seismic Methods at Madison Blue Spring State Park, Madison County, Florida. (Open Access Master's Thesis)Michigan Technological University. https://doi.org/10.37099/mtu.dc.etdr/152.

Brinkmann, R., Parise, M., Dye, D., 2008. Sinkhole distribution in a rapidly developing urban environment: Hillsborough County, Tampa Bay area, Florida. Eng. Geol. 99, 169–184. https://doi.org/10.1016/j.enggeo.2007.11.020.

Bumpus, P.B., Kruse, S.E., 2014. Self-potential monitoring for hydrologic investigations in urban covered-karst terrainSelf-potential monitoring. Geophysics 79, B231–B242. https://doi.org/10.1190/geo2013-0354.1.

Burke, B., Slee, A., McIntosh, P., Hofmann, H., Shulmeister, J., 2020. A reactivated cave system induces rapidly developing cover-collapse sinkholes in Tasmania, Australia. J. Cave Karst Stud. 81, 31–50. https://doi.org/10.4311/2019es0109.

Busetti, A., Calligaris, C., Forte, E., Areggi, G., Mocnik, A., Zini, L., 2020. Non-invasive methodological approach to detect and characterize high-risk sinkholes in urban cover evaporite karst: integrated reflection seismics, PS-InSAR, leveling, 3D-GPR, and ancillary data. A NE Italian case study. Remote Sens. 12, 3814. https://doi.org/10.3390/rs12223814.

Cahalan, M.D., Milewski, A.M., 2018. Sinkhole formation mechanisms and geostatistical-based prediction analysis in a mantled karst terrain. Catena 165, 333–344. https://doi.org/10.1016/j.catena.2018.02.010.

Carbonel, D., Rodríguez, V., Gutiérrez, F., McCalpin, J.P., Linares, R., Roqué, C., Zarroca, M., Guerrero, J., Sasowsky, I., 2014. Evaluation of trenching, ground penetrating radar (GPR) and electrical resistivity tomography (ERT) for sinkhole characterization. Earth Surf. Process. Landf. 39, 214–227. https://doi.org/10.1002/esp.3440.

Carbonel, D., Rodríguez-Tribaldos, V., Gutiérrez, F., Galve, J.P., Guerrero, J., Zarroca, M., Roqué, C., Linares, R., McCalpin, J.P., Acosta, E., 2015. Investigating a damaging buried sinkhole cluster in an urban area (Zaragoza city, NE Spain) integrating multiple techniques: geomorphological surveys, DInSAR, DEMs, GPR, ERT, and trenching. Geomorphology 229, 3–16. doi:doi: https://doi.org/10.1016/j.geomorph.2014.02.007

Cardarelli, E., Cercato, M., Donno, G.D., Filippo, G.D., 2014. Detection and imaging of piping sinkholes by integrated geophysical methods. Near Surf. Geophys. 12, 439–450. https://doi.org/10.3997/1873-0604.2013051.

Chalikakis, K., Plagnes, V., Guerin, R., Valois, R., Bosch, F.P., 2011. Contribution of geophysical methods to karst-system exploration: an overview. Hydrogeol. J. 19, 1169. https://doi.org/10.1007/s10040-011-0746-x.

Crosetto, M., Monserrat, O., Cuevas-González, M., Devanthéry, N., Crippa, B., 2016. Persistent scatterer interferometry: a review. ISPRS J. Photogramm. Remote Sens. 115, 78–89. https://doi.org/10.1016/j.isprsjprs.2015.10.011.

Dahm, T., Heimann, S., Bialowons, W., 2011. A seismological study of shallow, weak micro-earthquakes in the urban area of Hamburg city, Germany, and its possible relation to salt dissolution. Nat. Hazards 58, 1111–1134. https://doi.org/10.1007/s11069-011-9716-94.

Desir, G., Gutiérrez, F., Merino, J., Carbonel, D., Benito-Calvo, A., Guerrero, J., Fabregat, I., 2018. Rapid subsidence in damaging sinkholes: Measurement by high-precision leveling and the role of salt dissolution. Geomorphology 303, 393–409. https://doi.org/10.1016/j.geomorph.2017.12.004.

Doctor, D.H., Doctor, K.Z., 2012. Spatial analysis of geologic and hydrologic features relating to sinkhole occurrence in Jefferson County, West Virginia. Carbonates Evaporites 27, 143–152. https://doi.org/10.1007/s13146-012-0098-1.

Doctor, D., Young, J., 2013. An Evaluation of Automated GIS Tools for Delineating Karst Sinkholes and Closed Depressions From 1-Meter LiDAR-Derived Digital Elevation Data, pp. 449–458. https://doi.org/10.5038/9780979542275.1156.

Downs, Christine Marie, 2017. Imaging Wetland Hydrogeophysics: Applications of Critical Zone Hydrogeophysics to Better Understand Hydrogeologic Conditions in Coastal and Inland Wetlands and Waters. (Graduate Theses and Dissertations). https://scholarcommons.usf.edu/etd/7397.

Fabregat, I., Gutiérrez, F., Roqué, C., Comas, X., Zarroca, M., Carbonel, D., Guerrero, J., Linares, R., 2017. Reconstructing the internal structure and long-term evolution of hazardous sinkholes combining trenching, electrical resistivity imaging (ERI), and ground penetrating radar (GPR). Geomorphology 285, 287–304. https://doi.org/10.1016/j.geomorph.2017.02.024.

Fabregat, I., Gutiérrez, F., Roqué, C., Zarroca, M., Linares, R., Comas, X., Guerrero, J., Carbonel, D., 2019. Subsidence mechanisms and sedimentation in alluvial sinkholes inferred from trenching and ground penetrating radar (GPR). Implications for subsidence and flooding hazard assessment. Quat. Int. 525, 1–15. https://doi.org/10.1016/j.quaint.2019.09.008.

Ferretti, A., Savio, G., Barzaghi, R., Borghi, A., Musazzi, S., Novali, F., Prati, C., Rocca, F., 2007. Submillimeter accuracy of InSAR time series: experimental validation. IEEE Trans. Geosci. Remote Sens. 45, 1142–1153. https://doi.org/10.1109/tgrs.2007.894440.

Florea, Lee J., 2005. Using State-wide GIS data to identify the coincidence between sinkholes and geologic structure. J. Cave Karst Stud., 120–124. http://digitalcommons.wku.edu/geog_fac_pub/14.

Frumkin, A., Ezersky, M., Al-Zoubi, A., Akkawi, E., Abueladas, A.-R., 2011. The Dead Sea sinkhole hazard: geophysical assessment of salt dissolution and collapse. Geomorphology 134, 102–117. https://doi.org/10.1016/j.geomorph.2011.04.023.

Galve, J.P., Bonachea, J., Remondo, J., Gutiérrez, F., Guerrero, J., Lucha, P., 2008. Development and validation of sinkhole susceptibility models in mantled karst settings. A case study from the Ebro valley evaporite karst (NE Spain). Eng. Geol. 99 (3–4), 185–197. https://doi.org/10.1016/j.enggeo.2007.11.011.

Galve, J.P., Gutiérrez, F., Lucha, P., Guerrero, J., Bonachea, J., Remondo, J., Cendrero, A., 2009a. Probabilistic sinkhole modelling for hazard assessment. Earth Surf. Process. Landf. 34 (3), 437–452. https://doi.org/10.1002/esp.1753.

Galve, J.P., Gutiérrez, F., Lucha, P., Bonachea, J., Remondo, J., Cendrero, A., 2009b. Sinkholes in the salt-bearing evaporite karst of the Ebro River valley upstream of Zaragoza city (NE Spain) geomorphological mapping and analysis as a basis for risk management. Geomorphology 108 (3–4), 145–158. https://doi.org/10.1016/j.geomorph.2008.12.018.

Galve, J.P., Remondo, J., Gutiérrez, F., 2011. Improving sinkhole hazard models incorporating magnitude–frequency relationships and nearest neighbor analysis. Geomorphology 134 (1–2), 157–170. https://doi.org/10.1016/j.geomorph.2011.05.020.

Gómez-Ortiz, D., Martín-Crespo, T., 2012. Assessing the risk of subsidence of a sinkhole collapse using ground penetrating radar and electrical resistivity tomography. Eng. Geol. 149, 1–12. https://doi.org/10.1016/j.enggeo.2012.07.022.

Gutiérrez, F., Cooper, A.H., Johnson, K.S., 2008. Identification, prediction, and mitigation of sinkhole hazards in evaporite karst areas. Environ. Geol. 53, 1007–1022. https://doi.org/10.1007/s00254-007-0728-4.

Gutiérrez, F., Galve, J.P., Lucha, P., Castañeda, C., Bonachea, J., Guerrero, J., 2011. Integrating geomorphological mapping, trenching, InSAR, and GPR for the identification and characterization of sinkholes: a review and application in the mantled evaporite karst of the Ebro Valley (NE Spain). Geomorphology. https://doi.org/10.1016/j.geomorph.2011.01.018.

Gutiérrez, F., Zarroca, M., Linares, R., Roqué, C., Carbonel, D., Guerrero, J., McCalpin, J.P., Comas, X., Cooper, A.H., 2018. Identifying the boundaries of sinkholes and subsidence areas via trenching and establishing setback distances. Eng. Geol. 233, 255–268. https://doi.org/10.1016/j.enggeo.2017.12.015.

Gutiérrez, F., Benito-Calvo, A., Carbonel, D., Desir, G., Sevil, J., Guerrero, J., Martínez-Fernández, A., Karamplagidis, T., García-Arnay, Á., Fabregat, I., 2019. Review on sinkhole monitoring and performance assessment of the performance of remediation measures by high-precision leveling and terrestrial laser scanner in the salt karst of the Ebro Valley, Spain. Eng. Geol. 248, 283–308. https://doi.org/10.1016/j.enggeo.2018.12.004.

Healy, H. G., 1975. 'Terraces and Shorelines of Florida' [map]. 1:2000000. Map Series 71. Florida: Bureau of Geology, Florida Department of Natural Resources. Available at: https://ufdc.ufl.edu/UF90000326/00001

Hussain, Y., Uagoda, R., Borges, W., da S. Nunes, J.G., Hamza, O., Quispe, C.C., Aslam, K., Dou, J., Soto, M.C., 2020. (n.d.) The potential use of geophysical methods to identify cavities, sinkholes, and pathways for water infiltration: a case study from Mambaí, Brazil. https://doi.org/10.1002/essoar.10503456.2.

James, M.R., Robson, S., Smith, M.W., 2017. 3-D uncertainty-based topographic change detection with structure-from-motion photogrammetry: precision maps for ground control and directly georeferenced surveys. Earth Surf. Process. Landf. 42, 1769–1788. https://doi.org/10.1002/esp.4125.

Jardani, A., Dupont, J.P., Revil, A., 2006. Self-potential signals associated with preferential groundwater flow pathways in sinkholes. Journal of Geophysical Research Solid Earth 1978 2012 111. doi: https://doi.org/10.1029/2005jb004231

Jones, C.E., Blom, R.G., 2014. Bayou Corne, Louisiana, sinkhole: Precursory deformation measured by radar interferometry. Geology 42, 111–114. https://doi.org/10.1130/g34972.1.

Kaufmann, G., 2014. Geophysical mapping of solution and collapse sinkholes. J. Appl. Geophys. 111, 271–288. https://doi.org/10.1016/j.jappgeo.2014.10.011.

Kiflu, Henok Gidey, 2013. Optimized Correlation of Geophysical and Geotechnical Methods in Sinkhole Investigations: Emphasizing on Spatial Variations in West-Central Florida. Graduate Theses and Dissertations. https://scholarcommons.usf.edu/etd/4709.

Kim, J.-W., Lu, Z., Kaufmann, J., 2019. Evolution of sinkholes over Wink, Texas, observed by high-resolution optical and SAR imagery. Remote Sens. Environ. 222, 119–132. https://doi.org/10.1016/j.rse.2018.12.028.

Kruse, S., Grasmueck, M., Weiss, M., Viggiano, D., 2006. Sinkhole structure imaging in covered Karst terrain. Geophysical Research Letters 33. doi:doi: https://doi.org/10.1029/2006GL026975

Malinowska, A.A., Witkowski, W.T., Hejmanowski, R., Chang, L., van Leijen, F.J., Hanssen, R. F., 2019. Sinkhole occurrence monitoring over shallow abandoned coal mines with satellite-based persistent scatterer interferometry. Eng. Geol. 262, 105336. https://doi.org/10.1016/j.enggeo.2019.105336.

Mao, A., Harrison, C.G.A., Dixon, T.H., 1999. Noise in GPS coordinate time series. J. Geophys. Res. Atmos. 104, 2797–2816. https://doi.org/10.1029/1998jb900033.

Martel, R., Castellazz, P., Gloaguen, E., Trépanier, L., Garfias, J., 2018. ERT, GPR, InSAR, and tracer tests to characterize karst aquifer systems under urban areas: the case of Quebec City. Geomorphology 310, 45–56. doi:doi: https://doi.org/10.1016/j.geomorph.2018.03.003

Martínez-Moreno, F.J., Pedrera, A., Ruano, P., Galindo-Zaldívar, J., Martos-Rosillo, S., González-Castillo, L., Sánchez-Úbeda, J.P., Marín-Lechado, C., 2013. Combined microgravity, electrical resistivity tomography and induced polarization to detect deeply buried caves: Algaidilla cave (Southern Spain). Eng. Geol. 162, 67–78. https://doi.org/10.1016/j.enggeo.2013.05.008.

McClellan, M., Comas, X., Benscoter, B., Hinkle, R., Sumner, D., 2017. Estimating belowground carbon stocks in isolated wetlands of the northern everglades watershed, central Florida, using ground penetrating radar and aerial imagery. J. Geophys. Res. Biogeosciences 122 (11), 2804–2816. https://doi.org/10.1002/2016JG003573.

Miller, J. A., 1990. Ground Water Atlas of the United States [map]. 1:2500000. Hydrologic Atlas, 730-G, Segment-6, Alabama, Florida, Georgia, and South Carolina: U.S. Geological Survey. Pages 5, and 12-17. Available at: doi: https://doi.org/10.3133/ha730G.

National Elevation Dataset, 2011. US Geological Survey, https://nationalmap.gov/3DEP/.

Nof, R.N., Baer, G., Ziv, A., Raz, E., Atzori, S., Salvi, S., 2013. Sinkhole precursors along the Dead Sea, Israel, revealed by SAR interferometry. Geology 41, 1019–1022. https://doi.org/10.1130/g34505.1.

Nof, R.N., Abelson, M., Raz, E., Magen, Y., Atzori, S., Salvi, S., Baer, G., 2019. SAR interferometry for sinkhole early warning and susceptibility assessment along the Dead Sea, Israel. Remote Sens. 111, 89. https://doi.org/10.3390/rs11010089.

Oliver-Cabrera, Talib, 2018. InSAR Applications for Environmental and Hazard Monitoring. Open Access Dissertations. 2126. https://scholarlyrepository.miami.edu/oa_dissertations/2126.

Oliver-Cabrera, T., Wdowinski, S., Kruse, S., Robinson, T., 2020. InSAR detection of localized subsidence induced by sinkhole activity in suburban West-Central Florida. Proc. IAHS 382, 155–159. https://doi.org/10.5194/piahs-382-155-2020.

Oliver-Cabrera, T., Wdowinski, S., Kruse, S., Robinson, T., 2021. Detection of sinkhole activity in central Florida using InSAR time-series observations. Remote Sensing of Environment.

Osmanoğlu, B., Sunar, F., Wdowinski, S., Cabral-Cano, E., 2016. Time series analysis of InSAR data: methods and trends. ISPRS J. Photogramm. Remote Sens. 115, 90–102. https://doi.org/10.1016/j.isprsjprs.2015.10.003.

Ozdemir, A., 2015. Investigation of sinkholes spatial distribution using the weights of evidence method and GIS in the vicinity of Karapinar (Konya, Turkey). Geomorphology 245, 40–50. https://doi.org/10.1016/j.geomorph.2015.04.034.

Pazzi, V., Filippo, M.D., Nezza, M.D., Carlà, T., Bardi, F., Marini, F., Fontanelli, K., Intrieri, E., Fanti, R., 2018. Integrated geophysical survey in a sinkhole-prone area: Microgravity, electrical resistivity tomographies, and seismic noise measurements to delimit its extension. Eng. Geol. 243, 282–293. https://doi.org/10.1016/j.enggeo.2018.07.016.

Purdum, E.D., Fernald, E.A., 1998. Water Resources Atlas of Florida. Tallahassee: Institute of Science and Public Affairs. Florida State University, Tallahassee, pp. 40–41.

Puri, H.S., Vernon, R.O., 1959. Summary of the Geology of Florida and a Guidebook to the Classic Exposures (FGS: Special Publication 5). Bureau of Geology, Florida Department of Natural Resources, Tallahassee Available at: http://ufdc.ufl.edu/UF00000137/00001.

Rodgers, B.P.G., 2007. Conservation Coordinator for Sand Hill Scout Reservation. Unpublished work.

Rodriguez, V., Green, A. G., Carbonel, D., Horstmeyer, H., & Schmelzbach, C., 2014. Characterizing sagging and collapse sinkholes in a mantled karst by means of ground penetrating radar (GPR). Environmental & Engineering Geoscience, 109–132. doi: https://doi.org/10.2113/gseegeosci.20.2.109

Ronen, A., Ezersky, M., Beck, A., Gatenio, B., Simhayov, R.B., 2019. Use of GPR method for prediction of sinkholes formation along the Dead Sea Shores, Israel. Geomorphology 328, 28–43. https://doi.org/10.1016/j.geomorph.2018.11.030.

Scott, T. M., 2011. Geology of the Florida Platform. Gulf of Mexico Origin, Waters, and Biota: Volume 3, Geology, 17.

Scott, T. M., Campbell, K. M., Rupert F. R., Arthur J. D., Green R. C., Means G. H., Missimer T. M., Lloyd J. M., Yon, J. W., 2001. 'Geologic Map of the State of Florida (large)' [map]. 1: 750,000. Map Series 146. Florida Geological Survey, Tallahassee, Florida. https://geodata.dep.state.fl.us/datasets/FDEP::statemap-geology/about

Sevil, J., Gutiérrez, F., Zarroca, M., Desir, G., Carbonel, D., Guerrero, J., Linares, R., Roqué, C., Fabregat, I., 2017. Sinkhole investigation in an urban area by trenching in combination with GPR, ERT and high-precision leveling. Mantled evaporite karst of Zaragoza city, NE Spain. Eng. Geol. 231, 9–20. https://doi.org/10.1016/j.enggeo.2017.10.009.

Sevil, J., Benito-Calvo, A., Gutiérrez, F., 2021. Sinkhole subsidence monitoring combining terrestrial laser scanner and high-precision levelling. Earth Surf. Process. Landf. 46, 1431–1444. https://doi.org/10.1002/esp.5112.

Shi, Y., Tang, Y., Lu, Z., Kim, J.-W., Peng, J., 2019. Subsidence of sinkholes in Wink, Texas from 2007 to 2011 detected by time-series InSAR analysis. Geomatics, Natural Hazards and Risk 10, 1125–1138. doi:doi: https://doi.org/10.1080/19475705.2019.1566786

Soldo, B., Sivand, S.M., Afrasiabian, A., Đurin, B., 2020. Effect of Sinkholes on Groundwater Resources in Arid and Semi-Arid Karst Area in Abarkooh, Iran. Environ 7, 26. https://doi.org/10.3390/environments7040026.

Tihansky, A.B., 1999. Sinkholes, west-central Florida. In: Galloway, Devin, Jones, D.R., Ingebritsen, S.E. (Eds.), Land subsidence in the United States. 1182. U.S. Geological Survey Circular, pp. 121–140.

Tihansky, A.B., Knochenmus, L.A., 2001. Karst Features and Hydrogeology in west-central Florida—a field perspective. U.S. Geological Survey Karst Interest Group Proceedings. Retrieved from Water-Resources Investigations Report, pp. 198–211.

Upchurch, S., Scott, T.M., Alfieri, M.C., Fratesi, B., Dobecki, T.L., 2018. The karst systems of Florida, understanding karst in a geologically young terrain. Cave Karst Syst. World, 59–91. https://doi.org/10.1007/978-3-319-69635-5_3.

Westoby, M.J., Brasington, J., Glasser, N.F., Hambrey, M.J., Reynolds, J.M., 2012. 'Structure-from-Motion' photogrammetry: a low-cost, effective tool for geoscience applications. Geomorphology 179, 300–314. https://doi.org/10.1016/j.geomorph.2012.08.021.

Wright, E., Kruse, S., Forman, S., Harris, M.S., 2018. Millennial scale development of a southeastern United States spit. J. Coast. Res. 34, 255–271. https://doi.org/10.2112/JCOASTRES-D-16-00005.1.

Xiao, H., Kim, Y.J., Nam, B.H., Wang, D., 2016. Investigation of the impacts of local-scale hydrogeologic conditions on sinkhole occurrence in East-Central Florida, USA. Environ. Earth Sci. 75, 1274. https://doi.org/10.1007/s12665-016-6086-3.

Yechieli, Y., Abelson, M., Baer, G., 2015. Sinkhole formation and subsidence along the Dead Sea coast, Israel. Hydrogeol. J. 24 (3), 601–612. https://doi.org/10.1007/s10040-015-1338-y.

Youssef, A.M., Zabramwi, Y.A., Gutiérrez, F., Bahamil, A.M., Otaibi, Z.A., Zahrani, A.J., 2020. Sinkholes induced by uncontrolled groundwater withdrawal for agriculture in arid Saudi Arabia. Integration of remote-sensing and geophysical (ERT) techniques. J Arid Environ 177, 104132. doi: https://doi.org/10.1016/j.jaridenv.2020.104132

Zhou, W., Beck, B.F., Adams, A.L., 2002. Effective electrode array in mapping karst hazards in electrical resistivity tomography. Environ. Geol. 42, 922–928. https://doi.org/10.1007/s00254-002-0594-z.

Zhu, J., Taylor, T.P., Currens, C., Crawford, M.M., 2014. Improved karst sinkhole mapping in Kentucky using LiDAR techniques: a pilot study in Floyds Fork Watershed. J. Cave Karst Stud. 76, 207–216. https://doi.org/10.4311/2013es0135.

Zhu, J., Nolte, A.M., Jacobs, N., Ye, M., 2020. Using machine learning to identify karst sinkholes from LiDAR-derived topographic depressions in the Bluegrass Region of Kentucky. J. Hydrol. 588, 125049. https://doi.org/10.1016/j.jhydrol.2020.125049.

Zumpano, V., Pisano, L., Parise, M., 2019. An integrated framework to identify and analyze karst sinkholes. Geomorphology 332, 213–225. https://doi.org/10.1016/j.geomorph.2019.02.013.